

## Volcanic SiO<sub>2</sub>-cristobalite: A natural product of chemical vapor deposition

C. IAN SCHIPPER<sup>1,\*</sup>, WILLIAM D.A. RICKARD<sup>2</sup>, STEVEN M. REDDY<sup>2,3,†</sup>, DAVID W. SAXEY<sup>2</sup>,  
JONATHAN M. CASTRO<sup>4</sup>, DENIS FOUGEROUSE<sup>2</sup>, ZAKARIA QUADIR<sup>2</sup>, CHRIS CONWAY<sup>5</sup>,  
DAVID J. PRIOR<sup>6</sup>, AND KAT LILLY<sup>6</sup>

<sup>1</sup>School of Geography, Environment and Earth Sciences, Victoria University, P.O. Box 600, Wellington 6140, New Zealand

<sup>2</sup>John de Laeter Centre, Curtin University, GPO Box U1987, Perth, Western Australia 6845, Australia

<sup>3</sup>School of Earth and Planetary Sciences, Curtin University, GPO Box U1987, Perth, Western Australia 6845, Australia

<sup>4</sup>Institute for Geosciences, Johannes Gutenberg University, Mainz, Germany, 55099

<sup>5</sup>Geological Survey of Japan, AIST, 1-1-1 Higashi, Tsukuba, Ibaraki 305-8567, Japan

<sup>6</sup>Geology Department, University of Otago, P.O. Box 56, Leith Street, Dunedin 9016, New Zealand

### ABSTRACT

Cristobalite is a low-pressure, high-temperature SiO<sub>2</sub> polymorph that occurs as a metastable phase in many geologic settings, including as crystals deposited from vapor within the pores of volcanic rocks. Such vapor-phase cristobalite (VPC) has been inferred to result from silica redistribution by acidic volcanic gases but a precise mechanism for its formation has not been established. We address this by investigating the composition and structure of VPC deposited on plagioclase substrates within a rhyolite lava flow, at the micrometer to nanometer scale. The VPC contains impurities of the form [AlO<sub>4</sub>/Na<sup>+</sup>]<sup>0</sup>—coupled substitution of Al<sup>3+</sup> charge-balanced by interstitial Na<sup>+</sup>—which are typical of cristobalite. However, new electron probe microanalysis (EPMA) element maps show individual crystals to have impurity concentrations that systematically decline from crystal cores-to-rims, and atom probe tomography reveals localized segregation of impurities to dislocations. Impurity concentrations are inversely correlated with degrees of crystallinity [observed by electron backscatter diffraction (EBSD), hyperspectral cathodoluminescence, laser Raman, and transmission electron microscopy (TEM)], such that crystal cores are poorly crystalline and rims are highly ordered tetragonal  $\alpha$ -cristobalite. The VPC-plagioclase interfaces show evidence that dissolution-reprecipitation reactions between acidic gases and plagioclase crystals yield precursory amorphous SiO<sub>2</sub> coatings that are suitable substrates for initial deposition of impure cristobalite. Successive layers of cubic  $\beta$ -cristobalite are deposited with impurity concentrations that decline as Al-bearing gases rapidly become unstable in the vapor cooling within pores. Final cooling to ambient temperature causes a displacive transformation from  $\beta$ → $\alpha$  cristobalite, but with locally expanded unit cells where impurities are abundant. We interpret this mechanism of VPC deposition to be a natural proxy for dopant-modulated Chemical Vapor Deposition, where halogen-rich acidic gases uptake silica, react with plagioclase surfaces to form suitable substrates and then deposit SiO<sub>2</sub> as impure cristobalite. Our results have implications for volcanic hazards, as it has been established that the toxicity of crystalline silica is positively correlated with its purity. Furthermore, we note that VPC commonly goes unreported, but has been observed in silicic lavas of virtually all compositions and eruptive settings. We therefore suggest that despite being metastable at Earth's surface, cristobalite may be the most widely occurring SiO<sub>2</sub> polymorph in extrusive volcanic rocks and a useful indicator of gas-solid reaction having occurred in cooling magma bodies.

**Keywords:** Cristobalite, crystalline SiO<sub>2</sub>, atom probe, gas solid reaction, vapor phase mineralization, chemical vapor deposition, glass corrosion, rhyolite

### INTRODUCTION

Quartz is the nominally stable and most abundant silica (SiO<sub>2</sub>) polymorph in Earth's crust (Fig. 1a) but is typically found only in the most silicic of volcanic rocks (Bowen 1928; Gualda and Ghiorso 2013). Conversely, the low-pressure, high-temperature SiO<sub>2</sub> polymorph cristobalite can be found in lava flows and domes with compositions ranging from basaltic (e.g.,

Van Valkenburg and Buie 1945) to rhyolitic (e.g., Swanson et al. 1989). Efforts to understand volcanic cristobalite have been driven by the concern that it can exacerbate volcanic hazards, either by causing lung cancer or silicosis in people living near active volcanoes (e.g., Baxter et al. 1999), or by sealing permeable pathways in volcanic edifices and making them prone to explosive failure (e.g., Boudon et al. 2015). Furthermore, cristobalite has been recognized as a useful indicator of low-pressure degassing processes and gas-solid reactions in volcanic systems (e.g., Schipper et al. 2017).

Cristobalite is considered to be “metastable” when pre-

\* E-mail: ian.schipper@vuw.ac.nz; Orcid 0000-0002-9064-3370.

† Orcid 0000-0002-4726-5714.

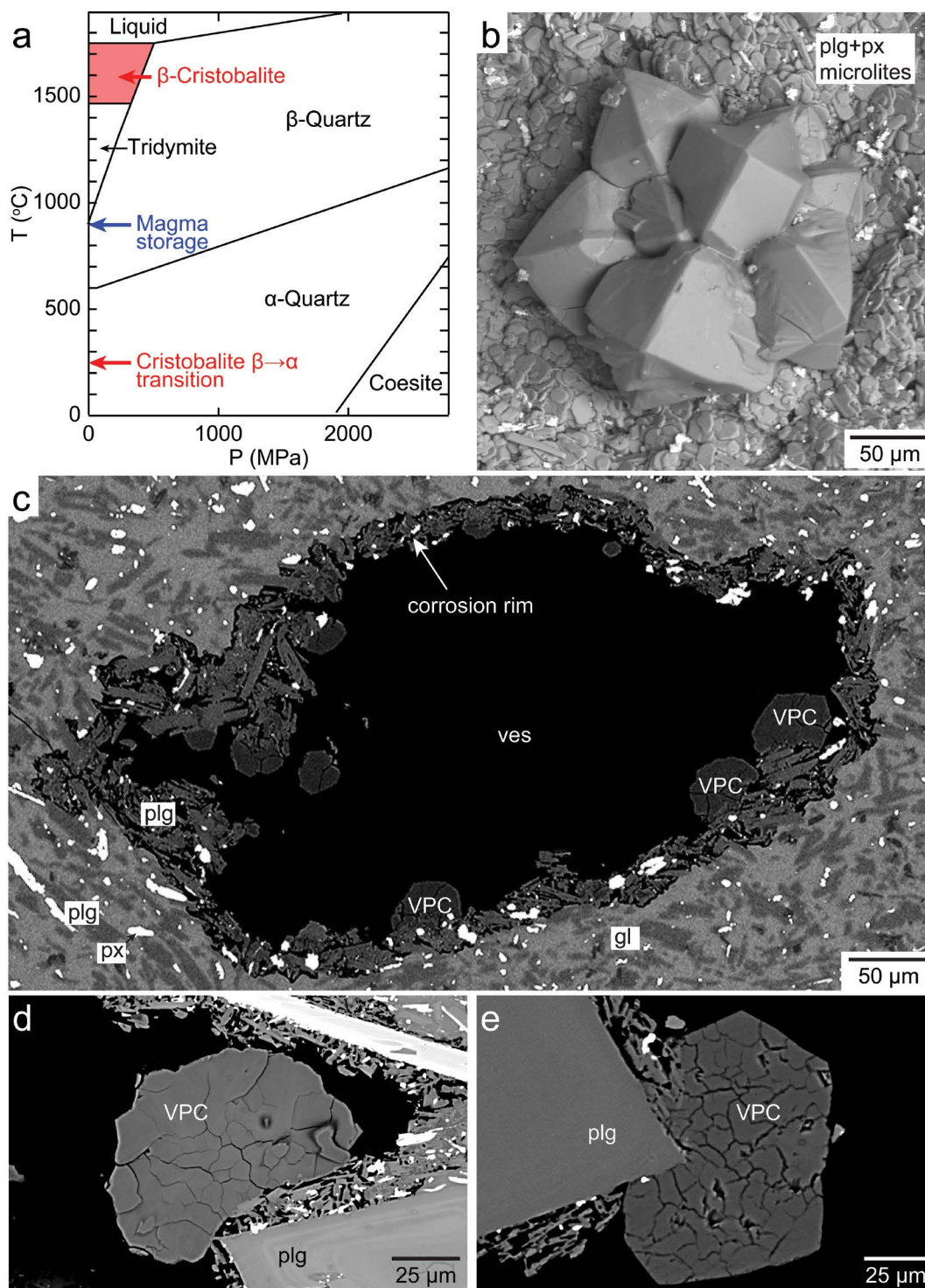


**FIGURE 1.** The SiO<sub>2</sub> system and vapor-phase cristobalite (VPC). (a) Low-pressure phase diagram for the silica system (modified from Heaney 1994). Note there is no stability field for  $\alpha$ -cristobalite, which is only metastable after the  $\beta \rightarrow \alpha$  transition at  $\sim 240$  °C. The pre-eruptive magma storage conditions at Cordon Caulle were at far lower temperature ( $\sim 900$  °C, 50 to 100 MPa; Castro et al. 2013) than the  $\beta$ -cristobalite stability field. (b) SEM image of a VPC crystal grown on a substrate that includes many plagioclase ( $\pm$  pyroxene) microlites. The microlites are clearly visible because any glass that was originally present has now been removed in the corrosion process. (c) BSE image of a VPC-bearing vesicle, with a glass-free corrosion rim and many VPC crystals. (d–e) BSE images in which characteristic fish scale cracking is apparent in VPC. Labels indicate vesicle (ves), plagioclase (plg), pyroxene (px), and VPC. All images are from Cordón Caulle lava samples, except (e), which is from an andesitic lava flow at Mt. Ruapehu, shown because the VPC crystal is clearly deposited on a plagioclase phenocryst. (Color online.)

served at ambient temperatures because these are outside its nominal stability field within the pure SiO<sub>2</sub> system (<0.2 MPa, 1470–1727 °C; Heaney 1994) (Fig. 1a). However, cristobalite is common at Earth's surface and has high- and low-temperature metastable forms: cubic  $\beta$ -cristobalite and tetragonal  $\alpha$ -cristobalite, with the  $\beta \rightarrow \alpha$  displacive transition occurring at ~240 °C (Horwell et al. 2013). It is often present as “stuffed derivatives,” with impurities incorporated into its relatively open structure (Buerger 1954). These impurities are usually of the form  $[\text{AlO}_4/\text{M}^+]^0$ , representing coupled substitution of  $\text{Al}^{3+}$  for  $\text{Si}^{4+}$  in Si-O tetrahedra, charge-balanced by interstitial monovalent cations ( $\text{M}^+ = \text{Na}^+, \text{K}^+, \text{Li}^+, \text{H}^+$ ) (Smith and Steele 1984). The presence of these impurities can prevent the reconstructive transformation to quartz during cooling to ambient temperature (Deer et al. 1992; Heaney 1994), can stabilize  $\beta$ - and  $\alpha$ -forms outside their stability fields (e.g., Perrotta et al. 1989; Chao and Lu 2002a), and can increase the size of unit cells and lower/broaden the temperature range of the  $\beta \rightarrow \alpha$  transition (Damby et al. 2014).

Volcanic cristobalite forms both by devitrification and by deposition from a vapor phase (Damby 2012; Horwell et al. 2013). Devitrification results in spherulites or altered groundmass glass in lava bodies and shallow intrusions (Swanson et al. 1989; Horwell et al. 2013). Devitrification is not the focus of this work but does contribute substantially to the total crystalline SiO<sub>2</sub> content of many volcanic rocks. In lava samples with high (>tens of weight percent) bulk cristobalite contents, most can be attributed to devitrification (Damby 2012; Schipper et al. 2015). Here, we focus on vapor-phase cristobalite (VPC), which occurs as idiomorphic crystals grown within the pores or vesicles of volcanic rocks (Horwell et al. 2013) (Figs. 1b–e). It is common for a given cristobalite-bearing volcanic rock to contain both devitrification and vapor-phase cristobalite. However, many VPC-bearing rocks retain glassy groundmasses with no signs of devitrification, so these forms of volcanic cristobalite are thought to form independently, but often concurrently (Schipper et al. 2015).

#### A GENERAL MECHANISM FOR VAPOR-PHASE CRISTOBALITE FORMATION

The working qualitative mechanism for VPC formation relies on the reactivity of acidic volcanic gases with aluminosilicate materials to explain VPC occurrences and textures (Damby 2012; Schipper et al. 2017). As magma cools at low pressures, halogens partition into aqueous fluids within pore networks to form acidic gas species [e.g., hydrofluoric (HF) and hydrochloric (HCl) acids] (Aiuppa et al. 2009; Schipper et al. 2019). These acidic gases can corrode/dissolve aluminosilicate material around pores (Oelkers 2001; Wolff-Boenisch et al. 2004), taking up silica and other elements into the vapor phase. Volatilized Si exists in the vapor in various forms, including as halogen complexes (e.g.,  $\text{SiCl}_4$ ,  $\text{SiF}_4$ ; de Hoog et al. 2005; Horwell et al. 2013). Both chlorine and fluorine are suitable ligands for Si, but HF is significantly more reactive than HCl. Unlike HCl, HF directly attacks Si-O bonds within aluminosilicate frameworks, and is therefore more efficient at corroding glass, and thought to be crucial for mobilizing SiO<sub>2</sub> (Schipper et al. 2017). Eventual deposition of SiO<sub>2</sub> as VPC is thought to occur when the vapor phase has become saturated in silica.

This mechanism has not yet been experimentally proven but does explain some key features of VPC occurrence and textures within established paradigms of volcanic degassing. First, slowly cooled magma bodies should have greater potential to produce VPC because the halogens required for SiO<sub>2</sub> mobilization exsolve from magmas that are emplaced at low-pressures in thermally insulated flows or domes, rather than by decompression during magma ascent (Aiuppa et al. 2009; Balcone-Boissard et al. 2010). This is reflected in the inverse correlation between lava extrusion rates and (sometimes) direct correlation between dome residence times and cristobalite contents of dome-derived tephra (Horwell et al. 2014). It also explains why VPC is sometimes found in the slowly cooled effusive, but not the rapidly quenched explosive, products of some volcanic eruptions (Schipper et al. 2015). Second, VPC-bearing pores in volcanic rocks often retain textural evidence that the corrosion process has occurred. Silicate minerals are more corrosion resistant than coexisting aluminosilicate glasses (Oelkers 2001), so the acid corrosion process rapidly removes glass from around pores, leaving behind identifiable lattice networks of silicate minerals in corrosion rims (de Hoog et al. 2005; Damby 2012; Schipper et al. 2015, 2017) (Figs. 1–2). Third, VPC has been found in association with halogen-rich secondary minerals (e.g., F-phlogopite) further suggesting an association with HF reactivity (de Hoog et al. 2005). The outstanding problem with the corrosion-deposition model is that it does not actually describe the deposition process of cristobalite. The deposition of VPC is assumed to have occurred based on its existence, but this remains the unexplained—and definitive—step in its formation.

To describe VPC formation as “vapor deposition” or “vapor mineralization” suggests some proxy for the chemical vapor deposition processes that are used in the industrial manufacture of thin-film devices (e.g., Pierson 1999; Foggia 2001). Interestingly, industrial deposition of SiO<sub>2</sub> films often uses Si-bearing source gases that are similar to those emitted from volcanoes (e.g.,  $\text{SiCl}_4$  or  $\text{SiF}_4$ ) (Klaus and George 2000; Nakahata et al. 2000). However, these are not directly comparable to volcanic scenarios because industrial Chemical Vapor Deposition is carried out with crystallographically appropriate substrates, under optimized conditions (e.g., pressures and temperatures), and/or using catalysts: all of which are chosen by engineers rather than dictated by nature. Still, there are fundamental challenges that any chemical vapor deposition process needs to overcome, which include but are not limited to: (1) finding or creating appropriate substrates onto which the desired films can be deposited; (2) overcoming barriers to deposition that are created by lattice mismatch between successive layers of film material; and (3) minimizing lattice strain in the resulting materials (Carlsson and Martin 2010). All of these barriers to vapor deposition must also be considered when describing the natural process of VPC formation in the pores of volcanic rocks.

Here, we take an in-depth look at the chemistry and structure of VPC from a rhyolite lava flow. Using a wide range of analytical tools, we investigate how compositional and microstructural characteristics of the VPC and their substrates can be explained by a mechanism that is a natural proxy for Chemical Vapor Deposition. We investigate nanostructural controls on VPC formation and discuss their implications for volcanic hazards and igneous petrology.

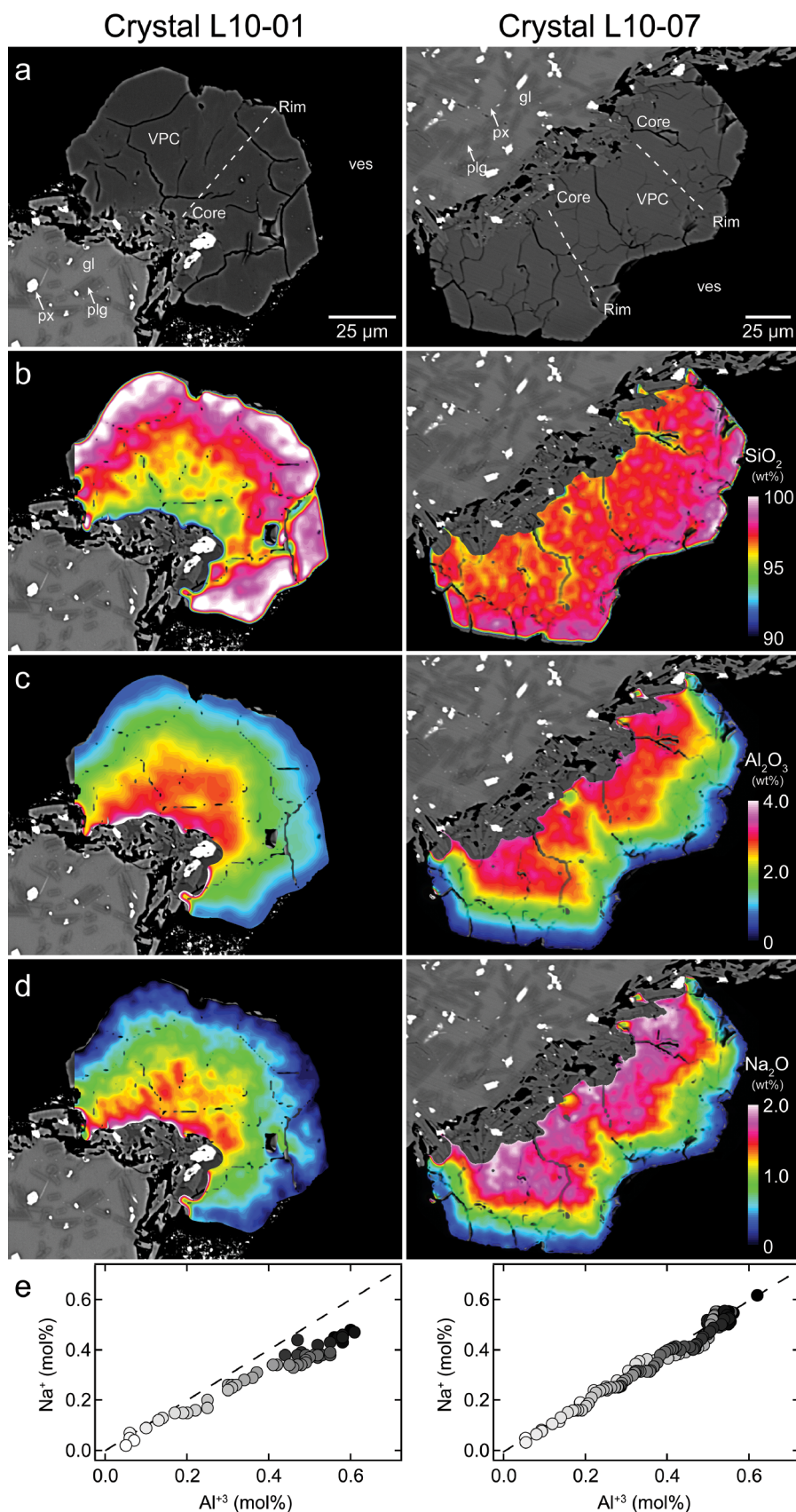


**FIGURE 2.** VPC major element chemistry by EPMA. (a) BSE images of singular (Crystal L10-01) and twinned (Crystal L10-07) VPC with phases marked as in Figure 1. (b–d) Maps of Si, Al, and Na, plotted as wt% oxides by convention. For clarity, only data within VPC crystals are shown. Ranges of each oxide are the same for both crystals. (e) Molar percentages of  $\text{Na}^+$  vs.  $\text{Al}^{3+}$ , with symbols colored according to position, darkening along the core-to-rim transects marked in a. The  $\text{Al}^{3+}/\text{Na}^+$  ratio of  $\sim 1$  confirms that these impurities are of the co-substitutional  $[\text{AlO}_4/\text{M}^+]^0$  form. Note that L10-01 was analyzed by EPMA before being analyzed by EBSD, and the opposite is true for L10-07. Uncertainties in EPMA analysis are smaller than symbol sizes. (Color online.)



## SAMPLES AND ANALYTICAL METHODS

### Samples

We examine natural VPC from the 2011–2012 rhyolite lava flow of Cordon Caulle volcano (Chile; and also make reference to unpublished data on VPC from andesites at Mt. Ruapehu, New Zealand). The 2011 Cordon Caulle eruption remains the largest subaerial volcanic eruption to-date of the 21st century. It distributed fine ash around the globe and produced lava with ~70 wt% SiO<sub>2</sub> (Castro et al. 2013; Tuffen et al. 2013; Schipper et al. 2019). The lava flow effused simultaneously with “hybrid” explosive activity from a common vent (Castro et al. 2013; Schipper et al. 2013). A previous systematic examination of Cordón Caulle eruption products showed cristobalite to be absent from all pyroclastic material, but present in all facies of the lava, locally accounting for up to ~23 wt% of the slowly cooled core of the lava flow (Schipper et al. 2015). The lava contains both devitrification and vapor-phase cristobalite, with the former being more abundant. We investigate individual VPC crystals from a selection of 33 Cordón Caulle lava samples (Schipper et al. 2015, 2019). The number of samples and individual VPC crystals analyzed by each technique varied as the investigation proceeded.

### Analytical methods

Whole VPC crystals from six different lava samples were observed by secondary electron microscopy (SEM) on unpolished rock chips with open vesicles. Images were collected with a JEOL 6610 SEM at Victoria University of Wellington, using 15 kV accelerating voltage and 8 nA beam current. All 33 lava samples were investigated in thin section using a flatbed scanner, petrographic microscope, and backscatter electron (BSE) imaging. BSE images were collected with the JEOL JXA-8230 Superprobe at Victoria University, using 15 kV accelerating voltage and 8 nA beam current. BSE imaging was used to select individual VPC crystals for analysis, targeting those that appeared to be cut sub-equatorially in the thin sectioning process. This ensured that analyses on a single polished surface captured material that is representative of both crystal cores and rims.

Major element compositions of VPC crystals were determined by several different applications of electron probe microanalysis (EPMA), using the JXA-8230 at Victoria University. One approach was to use wavelength dispersive spot analyses along core-to-rim transects across 23 different VPC crystals from seven different lava samples. Transects used 1  $\mu$ m spot size, 15 kV accelerating voltage, beam currents ranging from 2–12 nA, and peak/background counting times of 30/15 s. Another approach was to obtain EPMA element maps of 51 VPC crystals from seven lava samples. Maps used a focused beam, 15 kV, 12 nA, 0.5  $\mu$ m step size, and a short dwell time of only 400 ms. During mapping, only Si, Al, Na, K, and Ti were analyzed by wavelength dispersive spectroscopy, with a full suite of elements simultaneously collected by energy dispersive spectroscopy. Additional semi-quantitative analysis of more than 50 VPC crystals from ~20 samples was performed by energy dispersive spot analysis during sample investigation.

Hyperspectral cathodoluminescence (CL) spectra were obtained concurrently with EPMA maps, using a JEOL xCLent spectrometer installed in the optical pathway of the JXA-8230. At each pixel in the maps, CL intensities across a wavelength range of 350–1000 nm (3.542–1.240 eV) were collected simultaneously and processed using the xCLent Image software package.

Structure and orientation analysis of VPC crystals was carried out by electron backscatter diffraction (EBSD) at the University of Otago (Dunedin, New Zealand) and Curtin University (Perth, Australia). At Otago, EBSD patterns of 77 VPC crystals from four lava samples were obtained with a Zeiss Sigma VP FEGSEM fitted with an Oxford Instruments Nordlys camera. Crystals were analyzed using 30 kV, 50 nA, and a mapping step size of 500 nm. At Curtin, EBSD was performed on 20 crystals from a single lava sample using a Tescan MIRA VP-FEGSEM at 20 kV and ~1 nA, and step size of 200 nm. All analyses were undertaken at 70° tilt. Data were acquired using the Aztec software package version 3.3 and processed using Channel 5.12 software, both from Oxford Instruments. Match units for cristobalite were based on crystallographic data of Downs and Palmer (1994). EBSD map files were noise reduced using widspeke and 5-nearest-neighbor zero solution protocols.

Laser Raman analysis of 15 VPC crystals from five lava samples was performed using a Horiba JY LabRam HR800 at Victoria University. Raman analysis was performed in the backscattering configuration, with a 633 nm He-Ne laser for excitation, a holographic notch filter, a 600 mm<sup>-1</sup> grating, and a liquid-nitrogen cooled CCD detector. The laser power at the sample was 5 mW. Light was delivered and collected through an Olympus microscope objective with  $\times 100$  magnification (focal length 1.8 mm, NA 0.9), resulting in a probed area on the sample surface of approximately 1  $\mu$ m diameter. The spectral resolution was on the order of 3 cm<sup>-1</sup>, and spectra were integrated over a 10 s acquisition time.

Site specific samples for nanoscale compositional and structural analysis were extracted from areas of interest within VPC crystals using a Tescan Lyra3 Focused Ion Beam (FIB) SEM at Curtin University. The FIB-SEM used a Ga<sup>+</sup> ion source, and Pt deposition was used as a protective layer during high current milling.

Twenty needle shaped specimens from three VPC crystals were prepared for atom probe tomography (APT). These had lengths of ~2  $\mu$ m and tip diameters of ~100 nm and were extracted and mounted on prefabricated Si micro-tip coupons. Ion-beam milling of APT specimens was carried out at 30 kV with a final low-kilovolt (2 kV) milling step being used to minimize beam damage and Ga implantation. Trace and major element distributions at the nanoscale were investigated in 3D using the Cameca local electrode atom probe (LEAP) 4000X HR housed at the Geoscience Atom Probe facility at Curtin University, Australia. Atom probe data were manually ranged and reconstructed within Cameca's IVAS 3.8 software. Elemental abundances and spatial distributions in each specimen were also calculated with this software package.

A total of six foils from two VPC crystals were prepared for transmission electron microscopy (TEM). These were mounted onto a copper grid and thinned to 100 nm by FIB milling. TEM analysis was performed on an FEI Talos FS200X G2 TEM/scanning TEM (STEM) microscope operated at 200 kV and equipped with a Super-X EDS system located at Curtin University.

## RESULTS

### Textures

The cristobalite crystals on which we focus here are identical to those that have previously been described in the literature as the products of vapor-phase mineralization (Damby 2012; Horwell et al. 2013; Schipper et al. 2015). VPC is idiomorphic, which is typical for crystals having grown from a vapor, unconstrained by surrounding melt (Fig. 1b). The VPC host vesicles have typical corrosion rims (Fig. 1c), consisting of a lattice network of microlites, but free of interstitial glass (Damby 2012; Schipper et al. 2015). Crystals can approach ~100  $\mu$ m in size and usually have the characteristic “fish scale” cracking that is attributed to a volume reduction experienced during the ~240 °C displacive  $\beta$  (cubic)  $\rightarrow \alpha$  (tetragonal) transition (Horwell et al. 2013) (Figs. 1d–1e).

Our examination of VPC crystals in thin section shows them all to have contact with—or attachment to—one or more plagioclase crystal(s) at their bases. The specific plagioclase crystal(s) to which each VPC crystal is attached can be difficult to identify when VPC has grown onto a polycrystalline lattice of microlites (Fig. 1d). However, in rare cases where large plagioclase phenocrysts intersect pores, the attachment of VPC directly to plagioclase is clear (Fig. 1e).

### Major element composition

The results of EPMA spot analysis on Cordón Caulle VPC are summarized in Table 1, expressed by convention as element oxides. The VPC contains between 93.6–99.6 wt% SiO<sub>2</sub>.

**TABLE 1.** VPC composition by EPMA

wt%	Composition (wt%)			No. of spots/ No. of crystals
	Average	$\pm 1$ S.D.	Min–Max	
SiO <sub>2</sub>	97.4	1.15	93.6–99.6	827/12
TiO <sub>2</sub>	0.15	0.07	b.d.–0.37	831/12
Al <sub>2</sub> O <sub>3</sub>	1.74	0.88	0.19–4.17	829/12
FeO	0.09	0.10	b.d.–0.43	158/1
MgO	0.01	0.01	b.d.–0.04	157/1
CaO	0.05	0.04	b.d.–0.29	156/1
Na <sub>2</sub> O	0.64	0.64	b.d.–4.7	828/12
K <sub>2</sub> O	0.05	0.06	b.d.–0.45	830/12
P <sub>2</sub> O <sub>5</sub>	0.03	0.04	b.d.–0.15	159/1

Notes: Summary of spot analysis by EPMA. Data collected using focused beam, 15 kV accelerating voltage, and either 12 or 2 nA beam current. All spot analyses are thought to have suffered some loss of Na under electron radiation. b.d. refers to below detection limit.

The most abundant “impurities” (e.g., non-SiO<sub>2</sub> components) are Al<sub>2</sub>O<sub>3</sub> (0.19–4.17 wt%) and Na<sub>2</sub>O (0–4.7 wt%). The other major oxides that are common in silicate minerals (K<sub>2</sub>O, TiO<sub>2</sub>, CaO, MgO, FeO, P<sub>2</sub>O<sub>5</sub>) were only measured in one crystal, and in only trace amounts (<0.1 wt%) (Table 1). These results are similar to those of several other studies on volcanic cristobalite (Damby 2012; Horwell et al. 2012; Damby et al. 2013; Schipper et al. 2015, 2017). They suggest that impurity cations are of the expected co-substitutional  $[\text{AlO}_4/\text{M}^+]^0$  form (Buerger 1954), with sodium being the dominant interstitial monovalent cation ( $\text{M}^+ = \text{Na}^+$ ). However, we found sodium to be highly mobile under electron beam irradiation, and many of the spot analyses in this study (and previous studies by our group; Schipper et al. 2015, Schipper et al. 2017) are thought to have altered the initial Na<sub>2</sub>O concentrations (see below for further notes on beam damage). Potassium concentrations in VPC are low, despite  $[\text{AlO}_4/\text{K}^+]^0$  being common in the SiO<sub>2</sub> polymorph tridymite, which is also found in many volcanic rocks (Kayama et al. 2009a) but has not been found at Cordon Caulle. It is possible that the VPC also contains trace amounts of other monovalent cations (e.g., Li<sup>+</sup> or H<sup>+</sup>; Smith and Steele 1984), but these were not detected by EPMA analysis.

Compositional EPMA maps show impurities to systematically decline in concentration from crystal cores (at pore walls) to rims (Fig. 2). Similar core-to-rim increases in SiO<sub>2</sub> and decreases in Al<sub>2</sub>O<sub>3</sub> and Na<sub>2</sub>O were seen in all equatorially cut Cordon Caulle VPC crystals and were semi-quantitatively identified in >50 other VPC crystals from Cordon Caulle (and Mt. Ruapehu) by energy dispersive spot analysis. The short dwell time used in the EMPA mapping routine appears to have prevented or diminished the problem of Na migration that was encountered with EPMA spot analyses. It is by convention that the major elements are expressed as oxides, but when cast as cation moles along core-to-rim transects (Fig. 2e), it is apparent that the  $\text{Al}^{3+}/\text{Na}^+$  ratio is ~1 across a wide range of concentrations, as expected for co-substitutional  $[\text{AlO}_4/\text{Na}^+]^0$  impurities (Smith and Steele 1984).

### Micrometer-scale crystal structure

Electron backscatter diffraction was used to identify VPC crystals and study their microstructure. Cordon Caulle VPC exhibited very dramatic band contrast variation within crystals (Fig. 3a), which is a measure of the quality of the diffraction patterns during EBSD analysis (Prior et al. 2009). Crystal cores show weaker diffraction than crystal rims. Accordingly, indexing is poor in crystal cores, whereas crystal rims readily and exclusively index as tetragonal  $\alpha$ -cristobalite (Fig. 3b). Domain boundaries are dominantly parallel to  $\{101\}\alpha$  with others parallel to  $\{112\}\alpha$  (Fig. 3c). These (as well as the crystal cracking seen in BSE images) are consistent with the Cordon Caulle VPC having undergone a  $\beta \rightarrow \alpha$  transition. Boundaries parallel to  $\{101\}\alpha$  and  $\{112\}\alpha$  represent stacking faults inherited from dislocations on  $\{111\}\beta$ , and twins generated from reflection across  $\{101\}\beta$ , respectively (Christie et al. 1971).

Cathodoluminescence in silica polymorphs can arise from many different types of defects and/or incorporation of different impurities, some of which are still poorly constrained (Stevens-Kalceff et al. 2000). Hyperspectral CL maps of Cordon Caulle VPC also show core-to-rim variation (Fig. 3d). Crystals have

negligible luminescence (at any wavelength) in crystal cores but strong luminescence in crystal rims, with a peak at ~2.7 eV (459 nm) that is intrinsic to cristobalite (Moore and Karakus 1994).

Laser Raman spectra from crystal cores are featureless, while those from crystal rims have peaks at ~230 and ~417 cm<sup>-1</sup>. These vibrations are diagnostic of  $\alpha$ -cristobalite (Kingma and Hemley 1994) (Fig. 3e).

Cristobalite is known to be susceptible to beam damage under electron radiation, particularly when it is impure (Christie et al. 1971; Chao and Lu 2002a). Some analytical experimentation was required to determine the optimal way to capture all compositional and structural trends within VPC. In the examples shown in Figures 2 to 3, Crystal L10-01 was analyzed first by EPMA spot analysis at 12 nA and then at 2 nA, and was then repolished before analysis by EPMA mapping. Spot analyses yielded similar results in all elements except Na<sub>2</sub>O (results not shown but included in Table 1 summary), which was very low regardless of current, but substantial in EPMA maps (Fig. 2d). Despite re-polishing before subsequent analysis, 20 kV EBSD maps of Crystal L10-01 have tracks of obvious beam damage where spot analysis transects were performed and this crystal has completely unresolvable diffraction patterns in its core (Fig. 3). Conversely, Crystal L10-07 was analyzed first by 20 kV EBSD, and then by EPMA mapping. It still shows poor—but not completely unresolvable—diffraction pattern strength in its core, which is rich in Al<sub>2</sub>O<sub>3</sub> and Na<sub>2</sub>O. Initial EBSD tests using higher accelerating voltages of 30 kV (at University of Otago) resulted in significantly damaged crystals in which Al<sub>2</sub>O<sub>3</sub> concentrations were preserved but Na<sub>2</sub>O was almost completely lost. It appears that Na<sub>2</sub>O is indeed highly mobile under electron radiation and that cristobalite structure degrades during this process. However, EPMA and CL map data were collected simultaneously for all samples, and radial core-to-rim patterns of decreasing  $[\text{AlO}_4/\text{M}^+]^0$  and increasingly crystalline structure were observed in all the analyzed crystals. No detectable loss of Al<sub>2</sub>O<sub>3</sub> was apparent in any analyses, which is consistent with the  $\text{Al}^{3+}$  being substituted for  $\text{Si}^{4+}$  in the SiO<sub>2</sub> structure, rather than sitting in interstitial lattice sites. An additional analytical note is that regular core-to-rim variation in  $[\text{AlO}_4/\text{Na}^+]^0$  and the resulting structures will only be apparent if analyzing VPC crystals that are cut sub-equatorially to their growth axes.

### Atomic-scale distribution of impurities

The tendency for impurities to segregate to nanometer-scale dislocations and other such features has been shown analytically and computationally in various geological materials (e.g., Liu et al. 2016; Reddy et al. 2016), warranting an investigation of VPC at these scales by atom probe tomography. Two specimen tips from the core and four tips from the rim of one crystal yielded good results by APT, with  $>6 \times 10^6$  atoms detected (Table 2; Fig. 4a). The mass-to-charge ratio spectrum of cristobalite is relatively simple compared to other silicates (Fig. 4b). Silicon is present mainly as  $\text{Si}^+$ ,  $\text{Si}^{++}$ ,  $\text{Si}^{+++}$ ,  $\text{SiO}^+$ ,  $\text{SiO}^{++}$ ,  $\text{SiO}_2^+$ , and  $\text{SiO}_2^{++}$ . Aluminum was identified as  $\text{Al}^+$ ,  $\text{Al}^{++}$ ,  $\text{Al}^{+++}$ ,  $\text{AlO}^+$ , and  $\text{AlO}^{++}$ , while sodium was present as  $\text{Na}^+$ .

Bulk compositions of APT tips indicate the expected lower concentrations of Si and higher concentrations of Al in the crystal

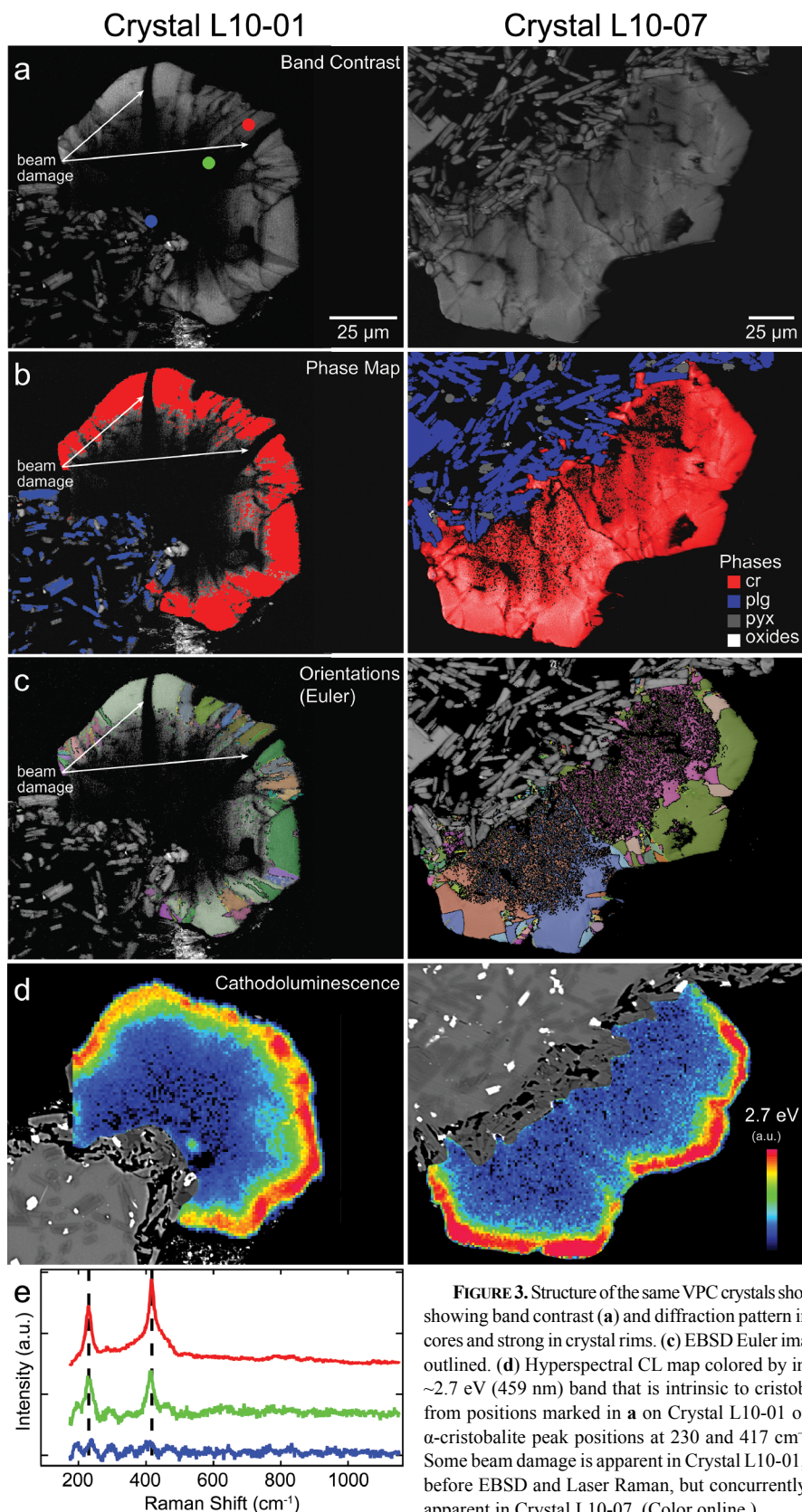


**TABLE 2.** VPC composition by APT

Liftout	AP-1 (core)			AP-2 (rim)		
APT run number	1037	1039	1344	1349	1361 <sup>a</sup>	1364
Atoms (×10 <sup>6</sup> )	13.6	35.4	20.0	13.7	8.8	6.3
at%						
Si	35.95	35.86	36.50	36.33	36.11	36.35
Ti	0.0039	0.0041	0.0041	0.0040	0.0034	0.0045
Al	0.836	0.985	0.257	0.303	0.330	0.339
CaO	0.0070	0.0101	0.0014	b.d.	b.d.	b.d.
Na	b.d.	b.d.	0.029	0.068	0.114	0.087
K	b.d.	b.d.	b.d.	b.d.	0.0031	b.d.
O	63.20	63.14	63.20	63.30	63.44	63.22

Notes: Bulk composition of the core and rim of a single VPC crystal (Fig. 4a) as determined by APT. <sup>a</sup> Tip 1361 contained the linear concentration of Al atoms illustrated in Figure 4d.

core compared to the crystal rim (Table 2; Fig. 4e). However, an unexpected result was that Na was below detection limit in specimens from the core and was in very low concentrations (<0.114 at%) in the rim. During data analysis, ranging of Na is complicated by a peak overlap between Na<sup>+</sup> and SiO<sup>2+</sup> at 23 Da, but this should cause an overestimation of Na concentrations in Si-rich material. We suspect the low Na concentrations to be the result of beam damage/Na loss that occurred prior to APT analysis, which for this crystal included EBSD at 30 kV, EPMA spot and map analysis, and FIB milling.

Tomographic reconstructions of APT data allow visualization of the spatial distribution of atoms in 3D (Figs. 4c–4d). Quali-

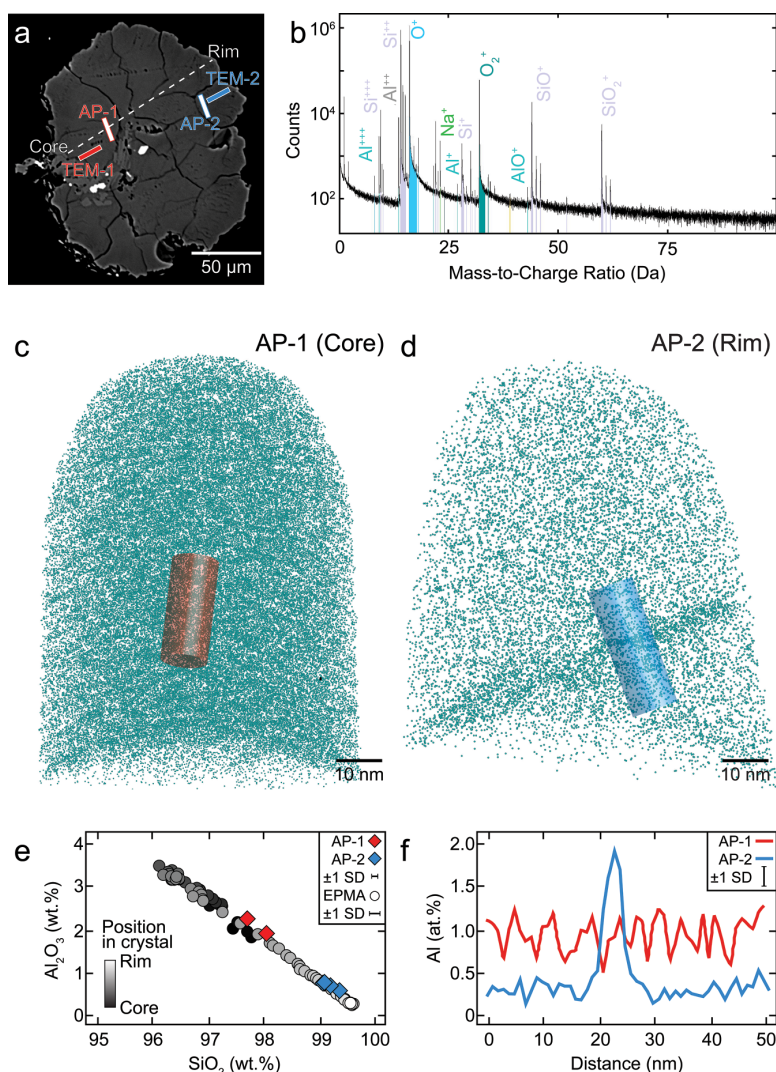


**FIGURE 4.** Composition of VPC by atom probe tomography. (a) VPC crystal showing liftout locations of APT specimen tips (and TEM foils; Fig. 5) from the core (AP-1, TEM-1) and rim (AP-2, TEM-2). Dashed white line marks EPMA spot analysis profile through this crystal. (b) Example of a ranged mass-to-charge ratio spectrum for VPC. (c–d) APT tomographic reconstructions showing 50% of Al atoms. Note the clustering of Al atoms in c and the Al-rich linear feature in d. (e) Plot of Al<sub>2</sub>O<sub>3</sub> vs. SiO<sub>2</sub> showing a good agreement between bulk APT analysis (Table 2) and EPMA spot analysis. To permit comparison, APT concentrations are converted from at% to equivalent wt% oxides by assuming ideal oxygen:cation ratios. (f) Linear Al concentration profiles taken along the cylinders shown in c–d, highlighting the apparent sawtooth concentration profiles created by Al clustering in the crystal core, and the Al-rich linear feature in the crystal rim. Average analytical uncertainties are shown as ±1 standard deviation (S.D.). (Color online.)



tatively, these show a heterogeneous distribution of Al atoms in crystal cores, with short order clustering. All specimens from the crystal rim appeared to have homogeneously distributed Al atoms, except for one (1361 in Table 2) where a 7–10 nm wide linear feature containing high concentrations of Al atoms was detected (Fig. 4d). Despite the apparent Na loss, comparison of Al concentrations from APT analysis (Table 2) and along EPMA spot analysis transects from the same crystal (Figs. 4a and 4e) indicate similar Al for a given Si concentration throughout the crystal (expressed as wt% oxides in Fig. 4e). Quantitative analysis of linear profiles using a small radius cylinder through the core volumes reveal them in fact to have sawtooth concentration profiles with a wavelength of 5–7 nm and magnitude of  $\pm 0.3$  at% Al (Fig. 4f). A linear concentration profile taken across the Al-rich feature in the crystal rim revealed it to have almost twice as much Al as seen anywhere in the crystal cores (Fig. 4f), despite the bulk Al concentration in crystal rims being at all times significantly lower than that in crystal rims.

#### Lattice structures within VPC and across the substrate-VPC interface

Two Cordon Caulle VPC crystals were examined by TEM, using bright-field and high-resolution imaging. Diffraction pat-

terns were obtained using fast Fourier transform (FFT) analysis of high-resolution TEM images.

The first crystal was the same one analyzed by APT (Fig. 4a) from which we used TEM to examine foils lifted from the crystal core and rim (Fig. 5). Bright-field images from the crystal core show low-contrast lamellae that varied in width from 12–50 nm (Fig. 5a), whereas images from the crystal rim had zones of mottled contrast and other zones of high-contrast lamellae at a finer scale of 6–12 nm (Fig. 5b). The lamellae in the crystal core (Fig. 5a) are similar to those that have been previously attributed to twin boundaries formed from stacking faults in cristobalite (Christie et al. 1971; Withers et al. 1989a, 1989b; Chao and Lu 2002a). No lattice fringes were observed in high-resolution images from regions around the twin structures in the crystal core, which in itself would suggest the material to be amorphous (Fig. 5c). However, FFT derived from these images (inset to Fig. 5c) have diffuse rings, the inner one at  $7.07 \pm 0.08$  Å, indicating that the VPC cores do contain some degree of short-range order (e.g., Eckert et al. 2015). The high-resolution images from the crystal rims have distinct lattice fringes indicating a well-developed crystalline structure, and the associated FFT have bright diffraction spots at  $6.92 \pm 0.02$  Å (Fig. 5d). The positions of the diffraction ring and spots in FFT from the core and rim are generally within the ranges expected

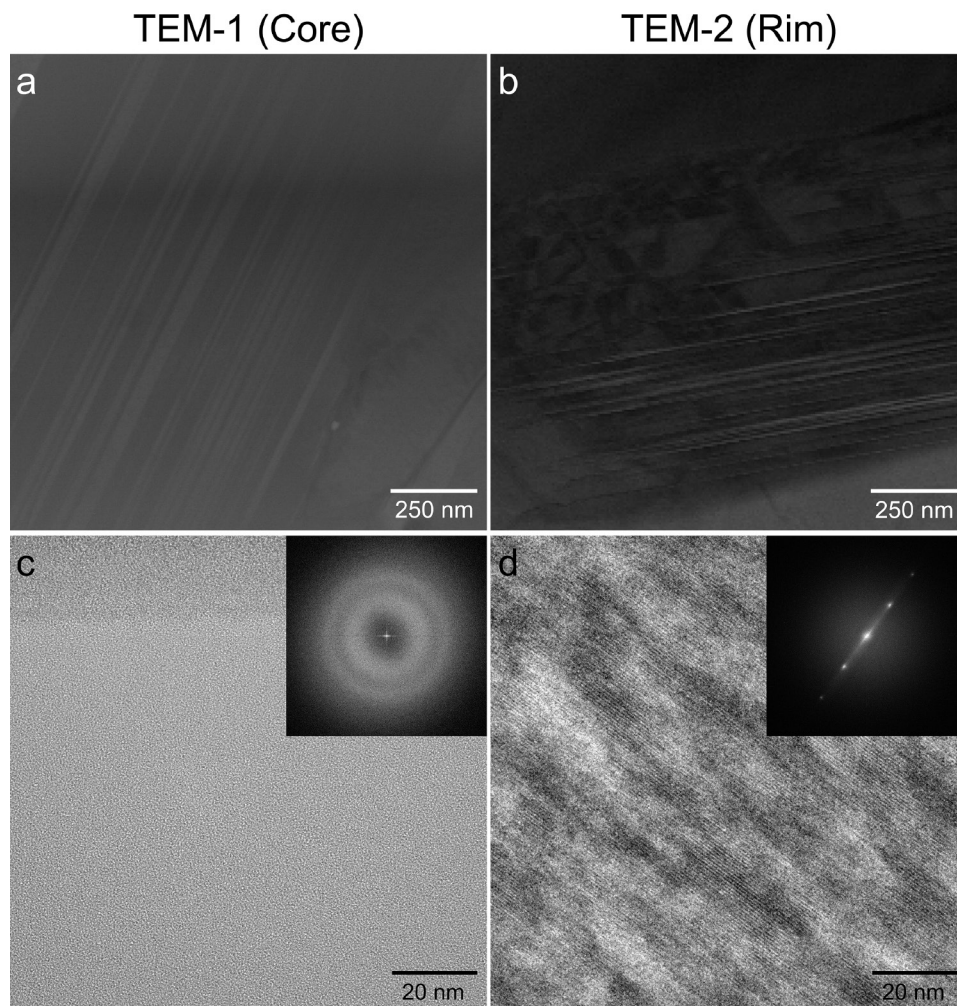


**FIGURE 5.** Structure of VPC observed by transmission electron microscopy. Foils are from the core (TEM-1; **a** and **c**) and rim (TEM-2; **b** and **d**) of the VPC crystal shown in Figure 4a. (**a** and **b**) Bright-field TEM images with lamellae typical of the stacking faults often seen in  $\alpha$ -cristobalite (Christie et al. 1971). (**c** and **d**) High-resolution images with inset FFT. Images from crystal core (**c**) appear amorphous, but their FFT have diffuse rings at  $7.07 \pm 0.08$  Å that suggest there to be some short-range order. Images from the crystal rim show well-defined crystal lattice fringes and have FFT with bright reflections at  $6.92 \pm 0.02$  Å.

for  $d(001)\alpha$  (i.e., the  $c$ -axis) of tetragonal  $\alpha$ -cristobalite (Deer et al. 1992). By assuming that distortion from an ideal tetragonal  $\alpha$ -cristobalite structure will be isotropic, the FFT data indicates the crystal core to have short-range order similar to  $\alpha$ -cristobalite but with an expanded  $d(101)\alpha$  of  $4.12 \pm 0.05$  Å, and the rim to have  $d(101)\alpha$  of  $4.04 \pm 0.01$  Å. All TEM analysis had to be performed with minimal beam exposure times, as rapid amorphization by the beam was apparent. This was particularly problematic in the impurity-rich crystal cores, whereas the crystal rims were notably more resistant to beam damage.

The other crystal investigated by TEM was selected because of its having a clearly identifiable plagioclase substrate crystal directly adjacent to the VPC core. This permitted a TEM foil to be cut perpendicularly across the plagioclase-VPC interface (inset to Fig. 6). High-resolution TEM images across the interface show distinct lattice fringes in plagioclase (confirmed by indexing of FFT, not shown). There is then an atomically sharp but slightly undulating interface with a material that lacks any indication of structure except for some slight mottled contrast, and appears similar to high-resolution TEM images of VPC cores (e.g., Fig. 5c). This amorphous material then meets a sharp interface with slightly darker but otherwise similar material. The interface between these two “amorphous” regions is at an angle of  $\sim 13^\circ$  to the plagioclase interface, so that the lighter one appears to be 36–43 nm wide within the frame of the images (Fig. 6). The darker contrast in the second amorphous layer could indicate that it has a slightly higher density or slightly more short-range order than the lighter amorphous layer.

## DISCUSSION

### Impurity distributions in vapor-phase cristobalite

Natural cristobalite is usually impure because it has a relatively open, low-pressure SiO<sub>2</sub> framework into which cations can readily substitute (Buerger 1954). The ranges of Al<sub>2</sub>O<sub>3</sub> and Na<sub>2</sub>O measured in Cordón Caulle VPC (Table 1, Fig. 2) are similar to those reported in volcanic cristobalite from other locations (Damby 2012; Horwell et al. 2012; Damby et al. 2013; Schipper et al. 2015; Schipper et al. 2017). Compositional heterogeneity has been previously noted in volcanic cristobalite (Damby 2012), but systematic core-to-rim variation has not been previously documented. The regular core-to-rim trend of decreasing impurities in equatorially cut VPC crystals (Fig. 2) was observed in every VPC crystal we investigated at Cordón Caulle, and also in VPC crystals from andesitic lava flows on Mt. Ruapehu (e.g., as in Fig. 1e), suggesting that the core-to-rim impurity profiles are not unique to select crystals, to Cordón Caulle, or to VPC in rhyolites.

The observed  $[\text{AlO}_4/\text{Na}^+]^0$  profiles cannot be explained by cation diffusion into—or out of—already-formed VPC. Aluminum diffusion rates in cristobalite are not specifically known, but are very slow in other forms of SiO<sub>2</sub> ( $10^{-24}$  m<sup>2</sup> s<sup>-1</sup> in quartz, Pankrath and Flörke 1994;  $10^{-22}$  m<sup>2</sup> s<sup>-1</sup> in amorphous SiO<sub>2</sub>, Francois-Saint-Cyr et al. 2003). Improbably long times (many millenia) would, therefore, be required to develop the observed profiles by diffusion. The profiles must, therefore, represent a temporal decline in  $[\text{AlO}_4/\text{Na}^+]^0$  incorporation during SiO<sub>2</sub> deposition. From a purely bulk perspective, there should be no shortage of Al<sup>3+</sup> and Na<sup>+</sup> available for incorporation into VPC. Compositional maps

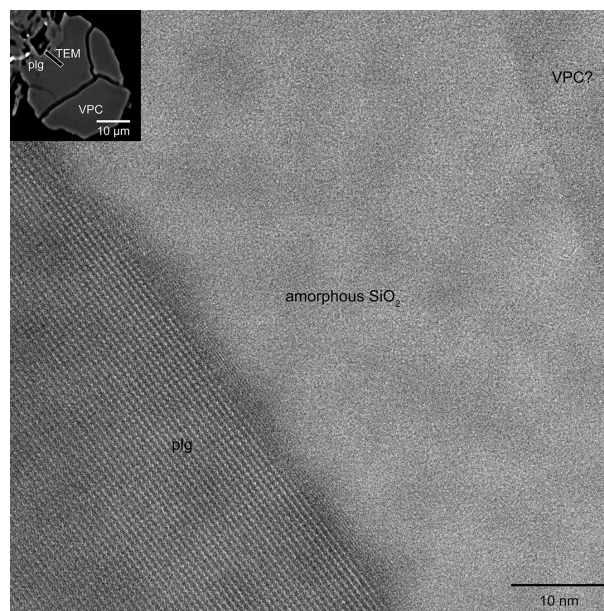


**FIGURE 6.** Substrate-VPC interface. High-resolution TEM image across the substrate-SiO<sub>2</sub> interface, with strong lattice fringes in the plagioclase substrate (plg), but amorphous structure in the adjacent SiO<sub>2</sub>. A region of slightly darker material (top right, marked “VPC?”) has a sharp interface with the amorphous SiO<sub>2</sub>. Inset is BSE image of VPC crystal, showing location of TEM foil.

of the groundmass around VPC-bearing pores in the Cordón Caulle lava flow by Schipper et al. (2015) did not show any evidence for diffusive depletion of Al or Na from groundmass glass. However, their work and the BSE images presented here show extensive evidence for stoichiometric dissolution of glass from around pores (Fig. 1c). This should volatilize substantial amounts of Al<sup>3+</sup> and Na<sup>+</sup> given that glass in the Cordón Caulle lava flow is rich in these elements ( $>13$  wt% Al<sub>2</sub>O<sub>3</sub> and  $>3$  wt% Na<sub>2</sub>O; Castro et al. 2013; Schipper et al. 2019). With no limit on the availability of impurity cations, there must be some other control on their incorporation into VPC.

The significance of the atomic-scale Al<sup>3+</sup> concentration profiles observed in impurity-rich VPC (Fig. 4f) is not clear, and to our knowledge, no appropriate proxies for cristobalite have been previously investigated by APT. Studies have used APT to demonstrate that impurity clumping can be linked to crystal growth kinetics in some minerals (e.g., Fougereuse et al. 2016; Wu et al. 2019), to document segregation of co-substituted trace elements in others (Reddy et al. 2016), and have shown B<sup>3+</sup> cations—which are identical in charge but of much smaller ionic radius than Al<sup>3+</sup>—to cluster in B-doped silicon (Blavette et al. 2010; Raghuvanshi et al. 2015). Perhaps more directly relevant to VPC are the similarly fine-scale chemical heterogeneities that have been documented in synthetically Al/Na-doped cristobalite (Chao and Lu 2002a), and the calculated geometric optimization studies that have shown Al<sup>3+</sup> to form clusters when substituting for Si<sup>4+</sup> in cristobalite (Liu et al. 2016). The impurity-poor VPC rims are mostly homogeneous at the atomic scale, except for in the one case where a  $\sim 7$ –10 nm wide Al<sup>3+</sup>-rich linear feature was observed (Figs. 4d and 4f). The significance of this feature is not

explicitly known, however, it is similar to features previously observed in APT data from various minerals (Piazolo et al. 2016; Kirkland et al. 2018; Fougere et al. 2019) and engineered materials (Blavette et al. 1999; Miller 2006) that have been interpreted as Cottrell atmospheres of trace elements decorating dislocations within crystal lattices.

### The link between impurities and crystal structure

The various individual techniques used to investigate VPC crystal structure all indicate an inverse relationship between  $[\text{AlO}_4/\text{M}^+]^0$  concentration and degree of crystallinity.

Weak EBSD diffraction patterns in impurity-rich crystal cores and robust patterns in impurity-poor crystal rims suggest a direct link between impurity concentrations and degree of long-range order in crystal frameworks (Fig. 3a). Comparison of  $[\text{AlO}_4/\text{Na}^+]^0$  distributions (Fig. 2) and EBSD maps (Figs. 3a–3c) suggest that ~2.5 wt%  $\text{Al}_2\text{O}_3$  marks a critical threshold, below which EBSD analysis confirms VPC to be highly crystalline  $\alpha$ -cristobalite, and above which VPC appears to be poorly crystalline or amorphous.

The CL intensity from cristobalite is known to decline during extended electron radiation (Kayama et al. 2009a). However, CL and EPMA mapping were concurrent in this work and performed with very short irradiation times. The observed core-to-rim variations in CL intensity are therefore not considered to be a result of beam damage. Our CL results contradict some previous interpretations of cristobalite luminescence. Kayama et al. (2009a) observed core-to-rim increases in CL intensity within natural VPC crystals from rhyolitic and andesitic lavas, identical to the patterns seen in VPC from Cordon Caulle (Fig. 3d). However, they attributed the luminescence to  $[\text{AlO}_4/\text{Na}^+]^0$  impurities, which would suggest that impurity-rich cores should show stronger luminescence than the impurity-poor rims. Our analysis suggests that this is not the case, and we note that the correlation between  $\text{Al}_2\text{O}_3$  concentration and CL intensity shown by Kayama et al. (2009a) is not only weak, it does not take into account spatial heterogeneity of  $\text{Al}_2\text{O}_3$  within VPC crystals, and does not include chemical analysis of their non-luminescent VPC cores. We note that poor luminescence can indicate that CL-active defects are sufficiently concentrated that radiative transitions are suppressed (“concentration quenching”; Götz 2012), or can be a consequence of the impurity-rich VPC cores being poorly crystalline or amorphous (Kayama et al. 2009a).

Laser Raman analysis is useful for discriminating between  $\text{SiO}_2$  polymorphs (e.g., Horwell et al. 2013). The featureless spectra from impurity-rich crystal cores (Fig. 3e) could mean they contain Raman-inactive  $\beta$ -cristobalite, or that they are poorly crystalline/amorphous, lacking the diagnostic  $\alpha$ -cristobalite peaks at ~230 and ~417  $\text{cm}^{-1}$  (Kingma and Hemley 1994), or even the ~400  $\text{cm}^{-1}$  peak sometimes seen in pure amorphous  $\text{SiO}_2$  (Bates 1972; Swainson et al. 2003).

Bright-field and high-resolution TEM images also suggest significant differences in the degrees of crystallinity within VPC cores and rims. The impurity-rich cores lack long-range order, appearing amorphous in high-resolution images (Figs. 5c and 6), but have FFT that indicate some degree of short-range order (inset to Fig. 5c) (Eckert et al. 2015). The impurity-poor VPC rims have a well-developed crystal lattice that is visible in high-resolution images and their FFT (Fig. 5d).

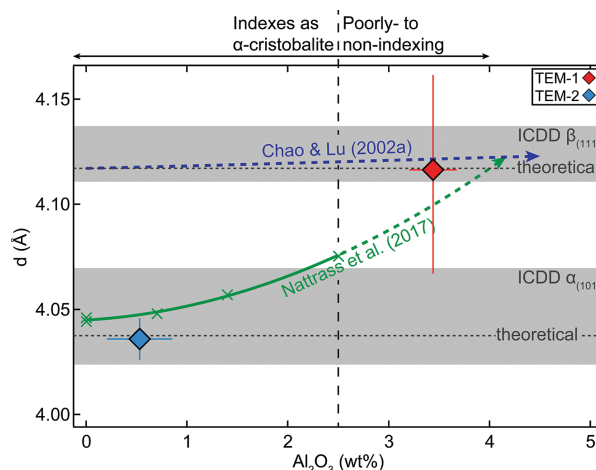


**FIGURE 7.** Influence of impurities on cristobalite lattice, with  $d(111)\beta$  and  $d(101)\alpha$  vs.  $[\text{AlO}_4/\text{M}^+]^0$  dopant concentration (expressed as wt%  $\text{Al}_2\text{O}_3$ ). Theoretical  $d$ -spacings calculated from lattice parameters for pure  $\text{SiO}_2$ -cristobalite (Deer et al. 1992), and ICDD ranges are replotted from Damby et al. (2014). Green crosses are Al/Na-doped  $\alpha$ -cristobalite from Natrass et al. (2017) with interpolated quadratic best-fit (solid green line,  $R^2 > 0.99$ ) extrapolated to ~4 wt%  $\text{Al}_2\text{O}_3$  (dashed green line). Impurities have a comparatively minor effect on  $d(111)\beta$  (Chao and Lu 2002a; after their data was adjusted for comparability, see text for explanation). The blue and red symbols represent data from the core (TEM-1) and rim (TEM-2) of the VPC crystal shown in Figures 4 to 5. (Color online.)

While some of the individual techniques for investigating cristobalite crystal structure can be interpreted in different ways, they all point to an inverse relationship between  $[\text{AlO}_4/\text{M}^+]^0$  concentration and crystal structure. Impurity-rich cores have some limited short range order, whereas the impurity-poor rims are highly crystalline, tetragonal  $\alpha$ -cristobalite.

### Impurity-modulated epitaxial deposition of cristobalite

The incorporation of  $[\text{AlO}_4/\text{M}^+]^0$  impurities are known to have significant effects on cristobalite structure and properties. Depending on their concentrations, these impurities can stabilize  $\beta$ -cristobalite to room temperature (Chao and Lu 2002a), which can result in  $\alpha$ -cristobalite with a unit cell that is expanded relative to that seen in pure  $\text{SiO}_2$  (Chao and Lu 2002b).

Previous work on the relationship between  $[\text{AlO}_4/\text{M}^+]^0$  concentrations (expressed as  $\text{Al}_2\text{O}_3$  wt%) and the size of cristobalite unit cells [as  $d(111)\beta$  and  $d(101)\alpha$ ] provide a framework for explaining our data on Cordon Caulle VPC (Fig. 7). Theoretical  $d$ -spacings for pure  $\text{SiO}_2$  are calculated from unit-cell dimensions given by Deer et al. (1992), and fall within the ranges that Damby et al. (2014) compiled from PDF-2 database cards from the International Centre for Diffraction Data (cf. Fig. 1 of Damby et al. 2014). The mild expansion of  $d(111)\beta$  with increasing  $\text{Al}_2\text{O}_3$  is derived from data given by (Chao and Lu 2002a). They reported X-ray diffraction data for synthetically Al/Na-doped  $\beta$ - and  $\alpha$ -cristobalite. Even at zero  $\text{Al}_2\text{O}_3$  the  $d$ -spacings they reported were vastly different to theoretical cristobalite lattice dimensions. To facilitate comparison with other data, we have fit a linear function to their data on  $\beta$ -cristobalite, but forced it

to intersect with the theoretical  $d(111)\beta$  at zero Al<sub>2</sub>O<sub>3</sub> (Deer et al. 1992). The more dramatic expansion of  $d(101)\alpha$  with increasing Al<sub>2</sub>O<sub>3</sub> is derived from data given by Nattrass et al. (2017). They reported 20 diffraction peak positions for synthetic Al/Na-doped  $\alpha$ -cristobalite with up to 2.5 wt% Al<sub>2</sub>O<sub>3</sub>. The  $d(101)\alpha$  calculated from their data can be fit extremely well to a quadratic function ( $R^2 > 0.99$ ) over the range of 0–2.5 wt% Al<sub>2</sub>O<sub>3</sub>.

As previously noted, Cordon Caulle VPC appears to be poorly crystalline/amorphous wherever Al<sub>2</sub>O<sub>3</sub> exceeds ~2.5 wt% (Figs. 2–3). Interestingly, extrapolation from the data of Nattrass et al. (2017) indicates that impurity concentrations  $\geq 2.5$  wt% Al<sub>2</sub>O<sub>3</sub> will result in  $\alpha$ -cristobalite with a unit cell that is larger than the normal range of  $d(101)\alpha$  (Fig. 7). The cores of natural VPC have higher impurity concentrations than investigated by Nattrass et al. (2017); however, EPMA and TEM data from the cores—and rims—of VPC (Figs. 5–6) plot within  $\pm 1\%$  of the quadratic curve to their data, even outside of their measurement ranges (Fig. 7). Although this is a limited data set, it suggests that the quadratic fit to the data of Nattrass et al. (2017) can be reliably extrapolated to higher impurity concentrations. Doing so suggests that the  $d(101)\alpha$  of highly impure  $\alpha$ -cristobalite should converge with the  $d(111)\beta$  of  $\beta$ -cristobalite when Al<sub>2</sub>O<sub>3</sub> approaches ~4 wt%, which approximates the maximum VPC impurity concentrations measured in this study (4.17 wt%; Table 1).

The “fish scale” cracking observed in BSE images (Figs. 1–2; Horwell et al. 2013) and grain orientations captured in EBSD (Fig. 3c; Christie et al. 1971) indicate that VPC was originally deposited as  $\beta$ -cristobalite and subsequently underwent a transition to  $\alpha$ -cristobalite upon cooling. Following from this, declining impurity concentrations allowed epitaxial lattice matching to proceed during VPC deposition and the subsequent transition (Fig. 7). A steady temporal decline in  $[\text{AlO}_4/\text{Na}^+]^0$  impurities within vapor-deposited layers of SiO<sub>2</sub> would ensure that at no point during deposition were lattice mismatches between subsequent layers sufficiently large to preclude deposition of the following layer. At high temperatures, unit-cell dimensions of  $\beta$ -cristobalite should have followed the gently sloping curve defined by data from Chao and Lu (2002a), with changes in  $[\text{AlO}_4/\text{Na}^+]^0$  creating negligible lattice strain. Following the  $\beta \rightarrow \alpha$  transition, only the regions with  $< 2.5$  wt% Al<sub>2</sub>O<sub>3</sub> are analytically identifiable as  $\alpha$ -cristobalite; however, even in regions with higher impurity concentrations, there is a regular continuum of distorted/expanded SiO<sub>2</sub> that grades into a poorly crystalline or partially amorphous proxy for  $\beta$ -cristobalite. This is consistent with the observations of Damby et al. (2014), who found natural VPC to have cell volumes between those of pure  $\alpha$ - and  $\beta$ -cristobalite. None of the VPC we examined appeared to contain remnants of stabilized  $\beta$ -cristobalite, but this is likely because  $[\text{AlO}_4/\text{Na}^+]^0$  concentrations in the natural VPC from Cordon Caulle were nowhere sufficient to fully stabilize  $\beta$ -cristobalite to room temperature (Perrotta et al. 1989; Saltzberg et al. 1992; Chao and Lu 2002a; Damby et al. 2014).

### Corroded substrates for initiation of vapor deposition

All observed VPC at Cordon Caulle is deposited on plagioclase (Figs. 1d–1e), which is enigmatic from the perspective of epitaxy. Although coordination of silica tetrahedra can permit thin-film cristobalite to grow on some highly dissimilar substrates

(Jewhurst et al. 2005), it is difficult to reconcile how cubic (or tetragonal) cristobalite could epitaxially bind to triclinic plagioclase without prohibitive angular and dimensional lattice misfits, despite the chemical similarity of these phases. Incorporation of  $[\text{AlO}_4/\text{M}^+]^0$  impurities themselves do modify the unit-cell dimensions of cristobalite (Fig. 7) but have minimal effect on high-temperature  $\beta$ -cristobalite (Chao and Lu 2002a). Furthermore, direct high-resolution TEM observations of plagioclase-SiO<sub>2</sub> boundaries in Cordon Caulle VPC do not show any evidence for epitaxy across the atomically sharp interfaces (Fig. 6).

The plagioclase-SiO<sub>2</sub> interfaces are identical to those attributed to “dissolution-reprecipitation” of silicate minerals, when acids stoichiometrically dissolve mineral surfaces and precipitate cation-depleted, amorphous SiO<sub>2</sub> layers over them (Hellmann et al. 2003; Lee et al. 2007; Hellmann et al. 2012). Unlike plagioclase itself, reprecipitated amorphous SiO<sub>2</sub> is an ideal substrate for sublimation of impurity-rich  $\beta$ -cristobalite, being structurally similar, except with a “static” instead of “dynamic” structure (Keen and Dove 1999). The interfaces observed by TEM furthermore have a sharp interface between lower- and higher-density regions in poorly crystalline SiO<sub>2</sub> (Fig. 6, and possibly also Fig. 5c). We speculate that this could be the actual interface between (1) reprecipitated plagioclase-derived amorphous SiO<sub>2</sub>; and (2)  $\beta$ -cristobalite (now preserved as impure and expanded  $\alpha$ -cristobalite) deposited from Si-saturated vapor.

Previous descriptions of VPC formation have identified glass dissolution as the source of SiO<sub>2</sub> (Damby 2012; Schipper et al. 2015, 2017), but have neglected how minerals—which are more resistant to corrosion, but not inert—are also affected by acidic vapor (Hellmann et al. 2003). Acidic vapor in a cooling lava body appears to play two complementary roles: corroding glass to provide a source of (impure) SiO<sub>2</sub> that is taken up into the vapor phase, while simultaneously modifying corrosion-resistant mineral surfaces to provide appropriate substrates for SiO<sub>2</sub> deposition from that same vapor. Formation of VPC is thus a natural proxy for impurity-modulated chemical vapor deposition, through a process that intrinsically provides its own impurity-modulated thin-film material while preparing its own appropriate substrate.

### Trace element transport in volcanic gases and the inferred temperatures of VPC formation

The previous sections describe how dissolution-reprecipitation of mineral surfaces can prepare the plagioclase substrate for vapor deposition of VPC, and how epitaxial lattice matching can occur between successive microlayers of SiO<sub>2</sub> with progressively declining  $[\text{AlO}_4/\text{Na}^+]^0$  concentrations (Fig. 7), but do not explain why  $[\text{AlO}_4/\text{Na}^+]^0$  impurities temporally decline during VPC deposition. Stoichiometric dissolution of volcanic glass with substantial Al<sub>2</sub>O<sub>3</sub> concentrations could in theory provide ample Al<sup>3+</sup> throughout the VPC deposition process, but this is not the case. We hypothesize that the temporal decline in  $[\text{AlO}_4/\text{Na}^+]^0$  impurities reflects the relative stability of metal-bearing gas species in volcanic systems.

Measurements and/or calculations on Al- and Si-bearing volcanic gas species are few in the literature, and those from rhyolitic systems are nonexistent. The general stability of various gas species from the well-studied Kudryavy volcano (Russia), however, can be used as a proxy for investigating the stability of different



species in high-temperature gases (Wahrenberger 1997; Churakov et al. 2000; Henley and Seward 2018) (Fig. 8). Churakov et al. (2000) identified four main Si-bearing and seven main Al-bearing species in high-*T* gases, leading Horwell et al. (2013) to suggest SiF<sub>4</sub> and/or SiCl<sub>4</sub> to be the main gases responsible for Si redistribution as VPC. The catalog of Si- and Al-bearing halogenated and/or hydroxylated gas species in high-*T* Kudryavy gases has subsequently been expanded as thermodynamic data has become available, permitting evaluation of gas-solid reactions with additional species [H<sub>4</sub>SiO<sub>4</sub>, Al(OH)<sub>3</sub>, and AlF(OH)<sub>2</sub>] that were not previously considered (Henley and Seward 2018) (Fig. 8).

The first item of note is that within the suite of halogen gases, fluorinated Si and Al complexes are vastly more stable than chlorinated ones in high-temperature volcanic gases (Fig. 8), which further supports the idea that HF is a necessary corroding agent and transportation precursor gas for VPC formation. During cooling of equilibrium volcanic gas from the Cordón Caulle eruption temperature (870–910 °C, Castro et al. 2013), all the investigated Al-bearing species quickly become unstable in the gas phase (Fig. 8). Most of the Si-bearing halides also become unstable, but the persistence of H<sub>4</sub>SiO<sub>4</sub> across a large temperature interval indicates that an Al-depleted bulk gas phase will still contain significant amounts of Si that is available for deposition of VPC. A rapid decline in all Al-bearing gas species during the isobaric cooling of volcanic gases in pores of the Cordón Caulle lava flow is therefore inferred to have increasingly limited Al availability in the vapor from which VPC was deposited, resulting in the observed core-to-rim decline in [AlO<sub>4</sub>/Na<sup>+</sup>]<sup>0</sup> impurities. Thus, the observed impurity distributions in Cordón Caulle VPC highlight the crudeness of bulk approaches that neglect the thermodynamics of gas-solid reactions in volcanic systems.

The actual temperature interval over which VPC forms is poorly constrained, but can be bracketed by various pieces of circumstantial evidence. The maximum temperature should be that of the magma storage conditions immediately before the eruption, petrologically defined as 870–910 °C by Castro et al. (2013). The absolute minimum temperature will be that of the β→α transition, which is nominally ~240 °C (Horwell et al. 2013), but is somewhat lower and over a broader interval in impure volcanic cristobalite (Damby et al. 2014). Field studies have shown that when ~1 m long silica tubes are placed in high-temperature fumaroles to generate a temperature gradient of ~900–500 °C along their full lengths, cristobalite is the first mineral to form at the hot end of the tubes (Le Guern and Bernard 1982; Symonds et al. 1987). This suggests that the minimum temperature of cristobalite deposition is much higher. The rapid deposition of cristobalite from high-temperature fumarolic gases has been attributed to the relatively low “volatility” (tendency to exist in the gas phase) of Si and the cations substituted into SiO<sub>2</sub> (Symonds et al. 1987) (e.g., Fig. 8). For comparison, several methods of industrial Chemical Vapor Deposition of SiO<sub>2</sub> thin films are often performed at ~400–450 °C (Foggiato 2001).

## IMPLICATIONS

### Implications for volcanic hazards

The potential importance of cristobalite was brought to the attention of the volcanological community when its presence was noticed in ash from Soufrière Hills Volcano, Montserrat

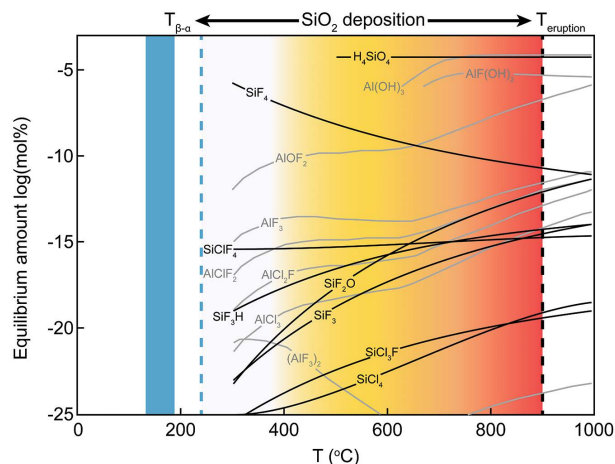


**FIGURE 8.** Equilibrium concentrations of Si- and Al-bearing halogen and hydroxyl volcanic gases, relative to inferred VPC formation and transition temperatures. Curves are calculated based on high-temperature gases from Kudryavy volcano (Henley and Seward 2018; Wahrenberger 1997), as a proxy for high-temperature volcanic gases in general. The temperature interval of SiO<sub>2</sub> deposition is bracketed by the Cordón Caulle eruption temperature (*T*<sub>eruption</sub> ~900 °C, Castro et al. 2013) and the β→α transition (lower/broader range for volcanic cristobalite (blue field); Damby et al. 2014, nominally ~240 °C (blue dashed line; Horwell et al. 2013). The red-to-yellow faded region indicates a more likely temperature range for VPC temperature based on field sampling of high-temperature fumaroles (Le Guern and Bernard 1982; Symonds et al. 1987). (Color online.)

(Baxter et al. 1999). Because cristobalite is toxic if inhaled, the concern was that people living near active volcanoes would be at high risk for developing chronic respiratory diseases (Horwell et al. 2012). Studies that have directly addressed the toxicity of volcanic cristobalite have found it to be less bio-reactive than some crystalline silica dusts, and this has been partly attributed to impurities within volcanic cristobalite (Horwell et al. 2003; Damby 2012; Horwell et al. 2012; Damby et al. 2016; Natrass et al. 2017). Natrass et al. (2017) directly addressed the relationship between [AlO<sub>4</sub>/Na<sup>+</sup>]<sup>0</sup> impurities and toxicity by preparing co-doped synthetic cristobalite and examining their reactivity in *in vitro* assays, finding that impurities reduce cristobalite’s toxicity.

Our new results on the distribution of [AlO<sub>4</sub>/Na<sup>+</sup>]<sup>0</sup> within VPC crystals adds an interesting note to the discussion of volcanic hazards. Stemming from the findings of Natrass et al. (2017), it appears that the SiO<sub>2</sub> concentration maps of VPC (Fig. 2a) can be considered analogous to maps of toxicity within individual crystals. Without detracting from the important issue of ascertaining that volcanic eruptions will not cause chronic lung diseases, we note that were an explosive event to fragment and mobilize the observed VPC into respirable plumes, it appears that only the fragments of crystal rims would be pure SiO<sub>2</sub>, and perhaps only these would be toxic.

### Implications for igneous petrology

It is worthwhile for igneous petrologists and volcanologists to look for VPC in lava flows and domes, because VPC formation requires corrosion of glass by halogen gases (Schipper et al. 2017). Its presence can, therefore, be taken as indicative that

a given magma body significantly degassed these potentially hazardous complexes during eruption (e.g., HF). Traditionally, however, vapor-phase cristobalite has often gone unrecognized. For example, although Mt. Ruapehu (New Zealand) lavas have been studied petrographically for many decades (Gregg et al. 1960; Cole 1978), the VPC that abounds within them (e.g., Fig. 1e) has only recently been noticed (Conway 2016). Despite being chronically underreported, VPC has been recognized in a vast array of volcanic rocks that differ in chemistry and setting. These range from basaltic lava flows of the Deccan Traps (Van Valkenburg and Buie 1945), to volcanic domes and dome-derived ash of many intermediate compositions (Baxter et al. 1999; Damby 2012; Boudon et al. 2015; Damby et al. 2016; Ivanova et al. 2018), to dacitic Vulcanian bombs (Schipper et al. 2017), to rhyolite lavas on land (Schipper et al. 2015), and in the deep sea (Ikegami et al. 2018; Manga et al. 2018). Furthermore, cristobalite (although not thought to be deposited from a vapor) is among the most common forms of silica in lunar and martian rocks (Miyahara et al. 2013; Kayama et al. 2018). We, therefore, suggest that cristobalite, while far from being the most abundant or nominally stable SiO<sub>2</sub> polymorph on Earth, may in fact be the most *widely occurring* SiO<sub>2</sub> polymorph in extrusive igneous rocks and a useful indicator of gas-solid reactions in volcanic systems.

## FUNDING

C.I.S. acknowledges a Faculty Strategic Research Grant from Victoria University of Wellington.

## REFERENCES CITED

- Aiuppa, A., Baker, D.R., and Webster, J.D. (2009) Halogens in volcanic systems. *Chemical Geology*, 263, 1–18. doi:10.1016/j.chemgeo.2008.10.005.
- Balcone-Boissard, H., Villemant, B., and Boudon, G. (2010) Behaviour of halogens during the degassing of felsic magmas. *Geochemistry, Geophysics, Geosystems*, 11, Q09005. doi:10.1029/2010GC003028.
- Bates, J.B. (1972) Raman spectra of  $\alpha$  and  $\beta$  cristobalite. *Journal of Chemical Physics*, 57, 4042–4047. doi:10.1063/1.1678878.
- Baxter, P.J., Bonadonna, C., Dupree, R., Hards, V.L., Kohn, S.C., Murphy, M.D., Nichols, A., Nicholson, R.A., Norton, G.E., Searl, A., Sparks, R.S.J., and Vickers, B.P. (1999) Cristobalite in volcanic ash of the Soufrière Hills Volcano, Montserrat, British West Indies. *Science*, 283, 1142–1145.
- Blavette, D., Cadel, E., Cococar-Miréduin, O., and Deconihout, B. (2010) The investigation of boron-doped silicon using atom probe tomography. *IOP Conference Series: Materials Science and Engineering*, 7, 012004. doi:10.1088/1757-899X/7/1/012004.
- Blavette, D., Cadel, E., Fraczkiewicz, A., and Menard, A. (1999) Three-dimensional atomic-scale imaging of impurity segregation to line defects. *Science*, 286, 2317–2319. doi:10.1126/science.286.5448.2317.
- Boudon, G., Balcone-Boissard, H., Villemant, B., and Morgan, D.J. (2015) What factors control superficial lava dome explosivity? *Scientific Reports*, 5, 14551. doi:10.1038/srep14551.
- Bowen, N.L. (1928) *The Evolution of the Igneous Rocks*. Princeton University Press, New Jersey.
- Buerger, M.J. (1954) The stuffed derivatives of the silica structures. *American Mineralogist*, 39, 600–614.
- Carlsson, J.-O., and Martin, P.M. (2010) Chemical vapor deposition. In P.M. Martin, Ed., *Handbook of Deposition Technologies for Films and Coatings*, p. 314–363. Elsevier, Amsterdam.
- Castro, J.M., Schipper, C.I., Amigo, A., Silva Parejas, C., Mueller, S., Jacob, D., and Miltzer, A.S. (2013) Storage and eruption of near-liquidus rhyolite magma at Cordon Caulle, Chile. *Bulletin of Volcanology*, 75, 702. doi:10.1007/s00445-013-0702-9.
- Chao, C.-H., and Lu, H.-Y. (2002a)  $\beta$ -cristobalite stabilization in (Na<sub>2</sub>O + Al<sub>2</sub>O<sub>3</sub>)-added silica. *Metallurgical and Materials Transactions A*, 33A, 2703–2711.
- (2002b) Stress-induced  $\beta$ - $\alpha$ -cristobalite phase transformation in (Na<sub>2</sub>O + Al<sub>2</sub>O<sub>3</sub>)-codoped silica. *Materials Science and Engineering A*, 328, 267–276.
- Christie, J.M., Lally, J.S., Heuer, A.H., Fisher, R.M., Griggs, D.T., and Radcliffe, S.V. (1971) Comparative electron petrography of Apollo 11, Apollo 12, and terrestrial rocks. *Proceedings of the Second Lunar Science Conference*, 1, 69–89.
- Churakov, S.V., Tkachenko, S.I., Korzhinskii, M.A., Bocharnikov, R.E., and Schmulovich, K.I. (2000) Evolution of composition of high-temperature fumarolic gases from Kudryavsky Volcano, Iturup, Kuril Islands: the thermodynamic modeling. *Geochemistry International*, 38, 436–451.
- Cole, J.W. (1978) Andesites of the Tongariro Volcanic Centre, North Island, New Zealand. *Journal of Volcanology and Geothermal Research*, 3, 121–153.
- Conway, C.E. (2016) Studies on the glaciovolcanic and magmatic evolution of Ruapehu Volcano, New Zealand. Ph.D. thesis, Victoria University of Wellington.
- Damby, D.E. (2012) From dome to disease: The respiratory toxicity of volcanic cristobalite. PhD thesis, Durham University, U.K.
- Damby, D.E., Llewellyn, E.W., Horwell, C.J., Williamson, B.J., Najorka, J., Cressey, G., and Carpenter, M. (2014) The  $\alpha$ - $\beta$  phase transition in volcanic cristobalite. *Journal of Applied Crystallography*, 47, 1205–1215. doi:10.1107/S160057671401070X.
- Damby, D.E., Murphy, F.A., Horwell, C.J., Raftis, J., and Donaldson, K. (2016) The in vitro respiratory toxicity of cristobalite-bearing volcanic ash. *Environmental Research*, 145, 74–84. doi:10.1016/j.envres.2015.11.020.
- de Hoog, J.C.M., van Bergen, M.J., and Jacobs, M.H.G. (2005) Vapour-phase crystallisation of silica from SiF<sub>4</sub>-bearing volcanic gases. *Annals of Geophysics*, 48, 775–785.
- Deer, W.A., Howie, R.A., and Zussman, J. (1992) *An Introduction to the Rock-Forming Minerals*, 2nd edition. Wiley, New York.
- Downs, R.T., and Palmer, D.C. (1994) The pressure behavior of  $\alpha$  cristobalite. *American Mineralogist*, 79, 9–14.
- Eckert, J., Gourdon, O., Jacob, D.E., Meral, C., Monteiro, P.J.M., Vogel, S.C., Wirth, R., and Wenk, H.-R. (2015) Ordering of water in opals with different microstructures. *European Journal of Mineralogy*, 27, 203–213.
- Foggia, J. (2001) Chemical vapor deposition of silicon dioxide films. In K. Seshan, Ed., *Handbook of Thin Film Deposition Processes and Techniques*, 2nd edition, p. 111–150. Elsevier, Amsterdam.
- Fougerouse, D., Reddy, S.M., Kirkland, C.L., Saxey, D.W., Rickard, W.D.A., and Hough, R.M. (2019) Time-resolved, defect-hosted, trace element mobility in deformed Witwatersrand pyrite. *Geoscience Frontiers*, 10, 55–63. doi:10.1016/j.gsf.2018.03.010.
- Fougerouse, D., Reddy, S.M., Saxey, D.W., Rickard, W.D.A., van Riessen, A., and Micklethwaite, S. (2016) Nanoscale gold clusters in arsenopyrite controlled by growth rate not concentration: Evidence from atom probe microscopy. *American Mineralogist*, 101, 1916–1919.
- Francois-Saint-Cyr, H.G., Stevie, F.A., McKinley, J.M., Elshot, K., Chow, L., and Trichardson, K.A. (2003) Diffusion of 18 elements implanted into thermally grown SiO<sub>2</sub>. *Journal of Applied Physics*, 94, 7433–7439. doi:10.1063/1.1624487.
- Götze, J. (2012) Application of cathodoluminescence microscopy and spectroscopy in geosciences. *Microscopy and Microanalysis*, 18, 1270–1284. doi:10.1017/S1431927612001122.
- Gregg, D.R., Grange, L.I., Williamson, J.H., Hurst, J.A., Clark, R.H. and Wilson, S.H. (1960) The geology of Rongararo subdivision. New Zealand Geological Survey, Lower Hutt.
- Gualda, G.A.R., and Ghiorso, M.S. (2013) Low-pressure origin of high-silica rhyolites and granites. *Journal of Geology*, 121, 537–545. doi:10.1086/671395.
- Heaney, P.J. (1994) Structure and chemistry of the low-pressure silica polymorphs. *Reviews in Mineralogy*, 29, 1–40.
- Hellmann, R., Penisson, J.-M., Hervig, R.L., Thomassin, J.-H., and Abrioux, M.-F. (2003) An EFTEM/HRTEM high-resolution study of the near surface of labradorite feldspar altered at acid pH: evidence for interfacial dissolution-precipitation. *Physics and Chemistry of Minerals*, 30, 192–197. doi:10.1007/s00269-003-0308-4.
- Hellmann, R., Wirth, R., Daval, D., Barnes, J.-P., Penisson, J.-M., Tisserand, D., Epicier, T., Florin, B., and Hervig, R.L. (2012) Unifying natural and laboratory chemical weathering with interfacial dissolution–reprecipitation: A study based on the nanometer-scale chemistry of fluid–silicate interfaces. *Chemical Geology*, 294–295, 203–216. doi:10.1016/j.chemgeo.2011.12.002.
- Henley, R.W., and Seward, T.M. (2018) Gas-solid reactions in arc volcanoes: Ancient and modern. *Reviews in Mineralogy and Geochemistry*, 84, 309–349. doi:10.2138/rmg.2018.84.9.
- Horwell, C.J., Fenoglio, I., Ragnarsdottir, K.V., Sparks, R.S.J., and Fubini, B. (2003) Surface reactivity of volcanic ash from the eruption of Soufrière Hills volcano, Montserrat, West Indies with implications for health hazards. *Environmental Research*, 93, 202–215. doi:10.1016/S0013-9351(03)00044-6.
- Horwell, C.J., Williamson, B.J., Donaldson, K., Le Blond, J.S., Damby, D.E., and Bowen, L. (2012) The structure of volcanic cristobalite in relation to its toxicity: relevance for the variable crystalline silica hazard. *Particle and Fibre Tech*, 9, 44.
- Horwell, C.J., Williamson, B.J., Llewellyn, E.W., Damby, D.E., and Le Blond, J.S. (2013) The nature and formation of cristobalite at the Soufrière Hills volcano, Montserrat: implications for the petrology and stability of silicic lava domes. *Bulletin of Volcanology*, 75, 696. doi:10.1007/s00445-013-0696-3.
- Horwell, C.J., Hillman, S.E., Cole, P.D., Loughlin, S.C., Llewellyn, E.W., Damby, D.E., and Christopher, T.E. (2014) Controls on variations in cristobalite abundance in ash generated by the Soufrière Hills Volcano, Montserrat in the

- period 1997–2010. *Geological Society of London Memoirs*, 39, 399–406. doi:10.1144/M39.21.
- Ikegami, F., McPhie, J., Carey, R., Mundana, R., Soule, A., and Jutzeler, M. (2018) The eruption of submarine rhyolite lavas and domes in the deep ocean—Hayre 2012, Kermadec Arc. *Frontiers in Earth Science*, 6, 147. doi:10.3389/feart.2018.00147.
- Ivanova, D.A., Shcherbakov, V.D., Plechov, P.Y., Nekrylov, N.A., Davydova, V.O., Turova, M.A., and Stepanov, O.V. (2018) Cristobalite in extrusive rocks of Bezymianny volcano. *New Data on Minerals*, 52, 51–58.
- Jewhurst, S.A., Andeen, D., and Lange, F.F. (2005) Crystal chemistry of the epitaxy of cristobalite (SiO<sub>2</sub>) on basal plane sapphire. *Journal of Crystal Growth*, 280, 168–172. doi:10.1016/j.jcrysgro.2005.03.031.
- Kayama, M., Nagaoka, H., and Niihara, T. (2018) Lunar and martian silica. *Minerals*, 8, 267. doi:10.3390/min8070267.
- Kayama, M., Nishido, H., and Ninagawa, K. (2009a) Effect of impurities on cathodoluminescence of tridymite and cristobalite. *Journal of Physics: Condensed Matter*, 104, 401–406.
- Kayama, M., Nishido, H., and Ninagawa, K. (2009b) Cathodoluminescence characterization of tridymite and cristobalite: Effects of electron irradiation and sample temperature. *American Mineralogist*, 94, 1018–1028. doi:10.2138/am.2009.3133.
- Keen, D.A., and Dove, M.T. (1999) Local structures of amorphous and crystalline phases of silica, SiO<sub>2</sub>, by neutron total scattering. *Journal of Physics: Condensed Matter*, 11, 9263–9273.
- Kingma, K.J., and Hemley, R.J. (1994) Raman spectroscopic study of microcrystalline silica. *American Mineralogist*, 79, 269–273.
- Kirkland, C.L., Fougereuse, D., Reddy, S.M., Hollis, J., and Saxey, D.W. (2018) Assessing the mechanisms of common Pb incorporation into titanite. *Chemical Geology*, 483, 558–566. doi:10.1016/j.chemgeo.2018.03.026.
- Klaus, J.W., and George, S.M. (2000) SiO<sub>2</sub> chemical vapor deposition at room temperature using SiCl<sub>4</sub> and H<sub>2</sub>O with an NH<sub>3</sub> catalyst. *Journal of the Electrochemical Society*, 147, 2658–2664. https://doi.org/10.1149/1.1393586.
- Le Guern, F., and Bernard, A. (1982) A new method for sampling and analyzing volcanic sublimates—Application to Merapi Volcano, Java. *Journal of Volcanology and Geothermal Research*, 12, 133–146.
- Lee, M.R., Brown, D.J., Smith, C. L., Hodson, M.E., MacKenzie, M., and Hellmann, R. (2007) Characterization of mineral surfaces using FIB and TEM: A case study of naturally weathered alkali feldspars. *American Mineralogist*, 92, 1383–1394. doi:10.2138/am.2007.2453.
- Liu, J., Wang, Y., and An, L. (2016) Abnormal behavior of silica doped with small amounts of aluminum. *Scientific Reports*, 6, 35556. doi:10.1038/srep35556.
- Manga, M., Mitchell, S.J., Degruyter, W., and Carey, R.J. (2018) Transition of eruptive style: Pumice raft to dome-forming eruption at the Havre submarine volcano, southwest Pacific Ocean. *Geology*, 46, 1075–1078. doi:10.1130/G45436.1.
- Miller, M.K. (2006) Atom probe tomography characterization of solute segregation to dislocations. *Microscopy Research and Technique*, 69, 359–365. doi:10.1002/jemt.20291.
- Miyahara, M., Kaneko, S., Ohtani, E., Sakai, T., Nagase, T., Kayama, M., Nishido, H., and Hirao, N. (2013) Discovery of seifertite in a shocked lunar meteorite. *Nature Communications*, 4, 1737. doi:10.1038/ncomms2733.
- Moore, R.E., and Karakus, M. (1994) Cathodoluminescence microscopy, a technique uniquely suited to the solution of refractory wear problems. *Proceedings of the International Ceramics Conference (Austceram'94)*, 925–940.
- Nakahata, K., Ro, K., Suemasu, A., Kamiya, T., Fortmann, C.M., and Smimizu, I. (2000) Fabrication of polycrystalline silicon films from SiF<sub>4</sub>/H<sub>2</sub>/SiH<sub>4</sub> gas mixture using very high frequency plasma enhanced chemical vapor deposition with in situ plasma diagnostics and their structural properties. *Japanese Journal of Applied Physics*, 39, 3294–3301. doi:10.1143/JJAP.39.3294.
- Natrass, C., Horwell, C.J., Damby, D.E., Brown, D., and Stone, V. (2017) The effect of aluminium and sodium impurities on the in vitro toxicity and pro-inflammatory potential of cristobalite. *Environmental Research*, 159, 164–175. doi:10.1016/j.envres.2017.07.054.
- Oelkers, E.H. (2001) General kinetic description of multioxide silicate mineral and glass dissolution. *Geochimica et Cosmochimica Acta*, 65, 3703–3719.
- Pankrath, R., and Flörke, O. W. (1994) Kinetics of Al-Si exchange in low and high quartz: calculation of Al diffusion coefficients. *European Journal of Mineralogy*, 6, 435–457. doi:10.1127/ejm/6/4/0435.
- Perrotta, A.J., Grubbs, D.K., Martin, E.S., Dando, N.R., McKinstry, H.A., and Huang, C.-Y. (1989) Chemical stabilization of β-cristobalite. *Journal of the American Ceramic Society*, 72, 441–447. doi:10.1111/j.1151-2916.1989.tb06150.x.
- Piazolo, S., La Fontaine, A., Trimby, P., Harley, S., Yang, L., Armstrong, R., and Cairney, J.M. (2016) Deformation-induced trace element redistribution in zircon revealed using atom probe tomography. *Nature Communications*, 7, 10490. doi:10.1038/ncomms10490.
- Pierson, H.O. (1999) *Handbook of Chemical Vapour Deposition*. Noyes Publications, Norwich, New York.
- Prior, D.J., Mariani, E., and Wheeler, J. (2009) EBSD in the Earth Sciences: Applications, Common Practice, and Challenges. In A.J. Schwartz, M. Kumar, B.L. Adams, and D.P. Field, Eds., *Electron Backscatter Diffraction in Materials Science*, p. 345–360. Springer, Switzerland.
- Raghuwanshi, M., Lanterne, A., Le Perche, J., Pareige, P., Cadel, E., Gall, S., and Duguay, S. (2015) Influence of boron clustering on the emitter quality of implanted silicon solar cells: an atom probe tomography study. *Progress in Photovoltaics: Research and Applications*, 23, 1724–1733. doi:10.1002/pip.2607.
- Reddy, S.M., van Riessen, A., Saxey, D.W., Johnson, T.E., Rickard, W.D.A., Fougereuse, D., Fischer, S., Prosa, T.J., Rice, K.P., Reinhard, D.A., Chen, Y., and Olson, D. (2016) Mechanisms of deformation-induced trace element migration in zircon resolved by atom probe and correlative microscopy. *Geochimica et Cosmochimica Acta*, 195, 158–170. doi:10.1016/j.gca.2016.09.019.
- Saltzberg, M.A., Bors, S.L., Bergna, H., and Winchester, S.C. (1992) Synthesis of chemically stabilized cristobalite. *Journal of the American Ceramic Society*, 75, 89–95.
- Schipper, C.I., Castro, J.M., Tuffen, H., James, M.R., and How, P. (2013) Shallow vent architecture during hybrid explosive-effusive activity at Cordon Caulle (Chile 2011–12): Evidence from direct observations and pyroclast textures. *Journal of Volcanology and Geothermal Research*, 262, 25–37. doi:10.1016/j.jvolgeores.2013.06.005.
- Schipper, C.I., Castro, J.M., Tuffen, H., Wadsworth, F.B., Chappell, D., Pantoja, A.E., Simpson, M., and Le Ru, E.C. (2015) Cristobalite in the 2011–12 Cordon Caulle eruption (Chile). *Bulletin of Volcanology*, 77, 34. doi:10.1007/s00445-015-0925-z.
- Schipper, C.I., Mandon, C., Maksimenko, A., Castro, J.M., Conway, C.E., Hauer, P., Kirilova, M., and Kilgour, G. (2017) Vapor-phase cristobalite as a durable indicator of magmatic pore structure and halogen degassing: An example from White Island volcano (New Zealand). *Bulletin of Volcanology*, 79, 74. doi:10.1007/s00445-017-1157-1.
- Schipper, C.I., Castro, J.M., Kennedy, B.M., Christenson, B.W., Aiuppa, A., Alloway, B.V., Forte, P., Seropian, G., and Tuffen, H. (2019) Halogen (Cl, F) and sulphur release during explosive, effusive, and intrusive phases of the 2011 rhyolitic eruption at Cordon Caulle volcano (Chile). *Volcanica*, 2, 73–90. doi:10.30909/vol.02.01.7390.
- Smith, J.V., and Steele, I.M. (1984) Chemical substitution in silica polymorphs. *Neues Jahrbuch Mineralogie Monatshefte*, 3, 137–144.
- Stevens-Kalceff, M.A., Phillips, M.R., Moon, A.R., and Kalceff, W. (2000) Cathodoluminescence microcharacterisation of silicon dioxide polymorphs. In M. Pagel, V. Barbin, P. Blanc, and D. Ohnenstetter, Eds. *Cathodoluminescence in Geosciences*, p. 193–223. Springer-Verlag, Berlin.
- Swainson, I.P., Dove, M.T., and Palmer, D.C. (2003) Infrared and Raman spectroscopy studies of the α-β transition in cristobalite. *Physics and Chemistry of Minerals*, 30, 353–365. doi:10.1007/s00269-003-0320-8.
- Swanson, S.E., Naney, M.T., Westrich, H.R., and Eichelberger, J.C. (1989) Crystallization history of Obsidian Dome, Inyo Domes, California. *Bulletin of Volcanology*, 51, 161–176.
- Symonds, R.B., Rose, W.L., Reed, M.H., Lichte, F.E., and Finnegan, D.L. (1987) Volatilization, transport and sublimation of metallic and non-metallic elements in high temperature gases at Merapi Volcano, Indonesia. *Geochimica et Cosmochimica Acta*, 51, 2083–2101.
- Tuffen, H., James, M.R., Castro, J.M., and Schipper, C.I. (2013) Exceptional mobility of an advancing rhyolitic obsidian flow at Cordon Caulle volcano in Chile. *Nature Communications*, 4, 2709. doi:10.1038/ncomms3709.
- Van Valkenburg, A., and Buie, B.F. (1945) Octahedral cristobalite with quartz paramorphs from Ellora Caves, Hyderabad State, India. *American Mineralogist*, 30, 526–535.
- Wahrenberger, C. (1997) Some aspects of the chemistry of volcanic gases. Ph.D. thesis, Swiss Federal Institute of Technology, Zurich.
- Withers, R.L., Thompson, J.G., and Welberry, T.R. (1989a) The structure and microstructure of α-cristobalite and its relationship to β-cristobalite. *Physics and Chemistry of Minerals*, 16, 517–523.
- Withers, R. L., Welberry, T.R., Hua, G.L., Thompson, J.G., and Hyde, B.G. (1989b) A transmission electron microscopy study of cristobalite. *Phase Transitions*, 16, 41–45. doi:10.1080/01411598908245678.
- Wolff-Boenisch, D., Gislason, S.R., and Oelkers, E.H. (2004) The effect of fluoride on the dissolution rates of natural glasses at pH 4 and 25°C. *Geochimica et Cosmochimica Acta*, 68, 4571–4582. doi:10.1016/j.gca.2004.05.026.
- Wu, Y.-F., Fougereuse, D., Evans, K.A., Reddy, S.M., Saxey, D.W., Guagliardo, P., and Li, J.-W. (2019) Gold, arsenic, and copper zoning in pyrite: A record of fluid chemistry and growth kinetics. *Geology*, 47, 641–644. doi:10.1130/G46114.1.

MANUSCRIPT RECEIVED JULY 31, 2019

MANUSCRIPT ACCEPTED NOVEMBER 10, 2019

MANUSCRIPT HANDLED BY AARON CELESTIAN